



SHADI PASSAM FATAYER

**TAILORING NANOSTRUCTURES OF TETRAPHENYL PORPHYRINS AND
PHTHALOCYANINES ON METALLIC SURFACES**

**CONSTRUÇÃO DE NANOESTRUTURAS DE PORFIRINAS E FTALOCIANINAS EM
SUPERFÍCIES METÁLICAS**

CAMPINAS

2014

i



**UNIVERSIDADE ESTADUAL DE CAMPINAS
INSTITUTO DE FÍSICA ‘GLEB WATAGHIN’**

SHADI PASSAM FATAYER

**CONSTRUÇÃO DE NANOESTRUTURAS DE PORFIRINAS E FTALOCIANINAS EM
SUPERFÍCIES METÁLICAS**

Orientador: Prof. Dr. Abner de Siervo

**TAILORING NANOSTRUCTURES OF TETRAPHENYL PORPHYRINS AND
PHTHALOCYANINES ON METALLIC SURFACES**

Dissertação de Mestrado apresentada ao Programa de Pós-Graduação em Física do Instituto de Física “Gleb Wataghin” da Universidade Estadual de Campinas para obtenção do título de Mestre em Física.

Masters dissertation presented to the Physics Postgraduate Program of the Institute of Physics “Gleb Wataghin” of the University of Campinas to obtain the M.Sc title in Physics.

ESTE EXEMPLAR CORRESPONDE À VERSÃO FINAL DA DISSERTAÇÃO
DEFENDIDA PELO ALUNO SHADI PASSAM FATAYER
E ORIENTADO PELO PROF. DR. ABNER DE SIERVO

Assinatura do Orientador

A handwritten signature in blue ink, written over a horizontal line. The signature is stylized and appears to be "Abner de Siervo".

**CAMPINAS
2014**

Ficha catalográfica
Universidade Estadual de Campinas
Biblioteca do Instituto de Física Gleb Wataghin
Valkíria Succi Vicente - CRB 8/5398

F268t Fatayer, Shadi Passam, 1989-
Tailoring nanostructures of tetraphenyl porphyrins and phthalocyanines on metallic surfaces / Shadi Passam Fatayer. – Campinas, SP : [s.n.], 2014.

Orientador: Abner de Siervo.
Dissertação (mestrado) – Universidade Estadual de Campinas, Instituto de Física Gleb Wataghin.

1. Auto-organização. 2. Porfirinas. 3. Ftalocianinas. 4. Microscopia de tunelamento de elétrons. I. Siervo, Abner de, 1972-. II. Universidade Estadual de Campinas. Instituto de Física Gleb Wataghin. III. Título.

Informações para Biblioteca Digital

Título em outro idioma: Construção de nanoestruturas de tetrafenil porfirinas e ftalocianinas em superfícies metálicas

Palavras-chave em inglês:

Self-organization

Porphyrins

Phthalocyanines

Scanning tunneling microscopy

Área de concentração: Física

Titulação: Mestre em Física

Banca examinadora:

Abner de Siervo [Orientador]

André Avelino Pasa

Alexandre Fontes da Fonseca

Data de defesa: 18-08-2014

Programa de Pós-Graduação: Física



MEMBROS DA COMISSÃO JULGADORA DA DISSERTAÇÃO DE MESTRADO DE
SHADI PASSAM FATAYER - RA 082792 APRESENTADA E APROVADA AO
INSTITUTO DE FÍSICA "GLEB WATAGHIN", DA UNIVERSIDADE ESTADUAL DE
CAMPINAS, EM 18 / 08 / 2014.

COMISSÃO JULGADORA:

Prof. Dr. Abner de Siervo - Orientador do Candidato
DFA/IFGW/UNICAMP

Prof. Dr. André Avelino Pasa – LFFS/DF/UFSC

Prof. Dr. Alexandre Fontes da Fonseca – DFA/IFGW/UNICAMP

ABSTRACT

The study of molecular systems on top of metal substrates has gathered increased attention of the scientific community. Better understanding over different self-assembly characteristics and the ability to control them in molecules has led to the development of quicker and cheaper routes of the use of the bottom-up approach in nanoscience.

Among the diverse studies, we can cite the development of gas sensors that use the magnetic signal of a self-assembled layer of molecules and the eventual binding of small molecules such as CO or NO leading to the emergence of magnetism on the sample. Another interesting aspect of the study of molecular systems is the similarity of molecules commonly used with molecules found in nature processes, e.g. chlorophylls and hemoglobins. This means that by studying simple molecules one can try to mimic the natural processes of those natural molecules.

In this sense, in our work we have studied two classes of molecules – Porphyrins and Phthalocyanines – and their structural properties when deposited on different metal substrates. The porphyrins were analyzed on a low-index miller surface, Cu(111) and compared to their behavior when deposited on vicinal substrates, Au(332) and Au(788). The porphyrins were observed to form 1D structures when deposited in small quantities depending on the nature of the substrate and its terrace width. At higher coverages, porphyrins formed different close-packed 2D structures, with square and parallelogram symmetry. Electronically was observed the modification of the chemical environment of nickel when NiTPP is adsorbed on Cu(111). The phthalocyanines were deposited on different substrates as well, towards the goal of producing co-assembling of two types of molecules as chessboard arrays. After the chessboard array was obtained we gathered knowledge about the mechanisms that formed such structures.

Towards the goal of studying molecular self-assembly, we have employed proper surface sensitive techniques such as Scanning Tunneling Microscopy, Scanning Tunneling Spectroscopy and X-Ray Photoelectron Spectroscopy. Such techniques allowed us to obtain the structural and electronic properties of the nanostructures formed.

Keywords: Self-organization. Porphyrins. Phthalocyanines. Scanning Tunneling Microscopy.

RESUMO

O estudo de sistemas moleculares em cima de substratos metálicos tem atraído uma crescente atenção da comunidade científica. O melhor entendimento sobre as características de auto-organização e a habilidade de controlá-las em moléculas tem gerado formas mais baratas e rápidas de usar a abordagem *bottom-up* em nanociência.

Dentre os diversos estudos feitos, podemos citar o desenvolvimento de sensores de gás que utilizam do sinal magnético de uma camada auto-organizada de moléculas e da ligação de pequenas moléculas como CO ou NO que promovem a emergência de magnetismo na amostra. Outro aspecto interessante do estudo de sistemas moleculares se encontra na similaridade das moléculas que podem ser utilizadas com moléculas encontradas nos processos recorrentes na natureza, por exemplo, as clorofilas e hemoglobinas. Isto significa que ao estudar moléculas simples é possível mimetizar um comportamento parecido com o das moléculas citadas.

Neste sentido, em nosso trabalho estudamos dois tipos de moléculas – Porfirinas e Ftalocianinas – e as propriedades estruturais quando depositadas em diferentes substratos metálicos. As porfirinas foram analisadas em uma superfície de baixo índice de Miller, Cu(111), e tiveram seu comportamento comparado com o análogo em superfícies vicinais, Au(332) e Au(788). As porfirinas formam estruturas em 1D quando depositadas em pequenas quantidades, dependendo da natureza do substrato e a largura de seu terraço. Em maiores coberturas, as porfirinas formam diferentes estruturas de empacotamento fechado em 2D, de simetrias quadrada e paralelogrâmica. Eletronicamente observou-se a modificação do entorno químico do níquel quando a molécula de NiTPP é adsorvida no Cu(111). As ftalocianinas foram depositadas em diferentes substratos visando a produção de co-organização de dois tipos de moléculas num padrão tabuleiro de xadrez. Após a obtenção do padrão de tabuleiro de xadrez, nós realizamos experimentos para elucidar os mecanismos que possibilitam formar tais estruturas.

Com o intuito de estudar auto-organização molecular, nós empregamos técnicas sensíveis a superfícies como a Microscopia de Tunelamento, Espectroscopia de Tunelamento e Espectroscopia de Fotoemissão por Raios-X. Tais técnicas possibilitam a obtenção das propriedades estruturais e eletrônicas das nanoestruturas formadas.

Palavras-chave: Auto-organização, Porfirinas, Ftalocianinas, Microscopia de Tunelamento de elétrons.

SUMMARY

1 INTRODUCTION.....	1
2 EXPERIMENTAL METHODS	4
2.1 SCANNING TUNNELING MICROSCOPY	4
2.1.1 Physical Principle	4
2.1.2 Scanning tunneling spectroscopy	8
2.1.3 I(z) spectroscopy	9
2.1.4 Molecular imaging with the STM	10
2.2 X-RAY PHOTOELECTRON SPECTROSCOPY	10
2.2.1 Physical principles	11
2.2.2 Chemical Shift.....	13
2.3 MOLECULAR EPITAXY	14
3 NICKEL TETRAPHENYL PORPHYRINS ON LOW INDEX AND VICINAL METAL SURFACES.....	16
3.1 INTRODUCTION.....	16
3.2 NICKEL TETRAPHENYL PORPHYRINS.....	17
3.3 NITPP ON CU(111)	19
3.3.1 Cu(111) surface	19
3.3.2 One dimensional molecular adsorption	19
3.3.3 Transition between disordered one-dimensional and ordered two dimensional adsorption	21
3.3.4 Two dimensional assembly and chirality	23
3.3.5 XPS analysis of NiTPP/Cu(111)	25
3.4 NITPP ON VICINAL GOLD	28
3.4.1 Vicinal surfaces	28
3.4.2 Submonolayer adsorption of NiTPP on vicinal Au	32
3.4.3 Mono and multilayer coverage on vicinal Au	34
3.5 CONCLUSION OF NITPP ON DIFFERENT METALLIC SUBSTRATES	38
4 BIMOLECULAR MIXTURE OF PHTHALOCYANINES	40
4.1 INTRODUCTION.....	40
4.2 PHTHALOCYANINES	41

4.3 TENTATIVE MOLECULAR SORTING ON SILVER (111) AND COPPER (100)	42
4.4 ANALYSIS OF SURFACE OF BISMUTH ON TOP OF COPPER (100)	43
4.5 COMPARISON BETWEEN SINGLE MOLECULE ISLANDS AND BIMOLECULAR MIXTURES.....	46
4.6 CONCLUDING REMARKS.....	54
5 CONCLUSION AND PERSPECTIVES	56
6 REFERENCES.....	58

ACKNOWLEDGEMENTS/AGRADECIMENTOS

Venho por meio desta seção agradecer a todas as pessoas que fizeram parte indiretamente de meus anos como aluno da UNICAMP, desde 2005 até 2013. Como disse Bilbo Baggins “Gostei de metade de vocês menos da metade que vocês mereciam”, e neste sentido também me desculpo um pouco.

Agradeço as pessoas que foram essenciais em minha formação, começando na graduação posso citar os professores Ricardo Mosna, Silvio Vitiello, José Brum e a falecida Professora Kyoko Furuya. Além da sala de aula, também tive a ótima oportunidade de estar em contato diário com o Professor Lisandro Pavie Cardoso durante meu estágio como Técnico em mecânica em 2008. Durante os três últimos anos de graduação tive a inestimável experiência de ter sido orientado pelos Professores Daniel Mário Ugarte e Varlei Rodrigues, e a eles sempre serei grato por todas as lições aprendidas.

Gostaria de dedicar este parágrafo ao meu orientador, Professor Abner de Siervo e ao grupo de Física de Superfícies. Me acolheram sem ressalvas no início de meu mestrado e desde o começo sempre me senti muito bem neste grupo. Neste contexto, devo muito ao Professor Richard Landers por sempre se mostrar solícito para com as minhas (às vezes repetitivas) dúvidas e sempre apresentar interesse sobre o meu andamento com relação ao projeto. Agradeço também aos colegas Mauricio, Guilherme, Emilia, Caio e Luis. Também sou grato aos funcionários do grupo, Therezinha, Rita, Idalício e Edson pelo ótimo ambiente e ajudas prestadas. Voltando ao Professor Abner, sou grato por sempre ter me fornecido todo o empurrão necessário para avançar na área de Física de Superfícies e ter incentivado que eu passasse um período do mestrado na Suíça – uma experiência que mudou, moldou e moldará minha carreira em Ciências Físicas.

Agradeço aos incansáveis amigos: Lord Kevin, John, Caesar, Hector, Eric, Miranda, Stephanie, Débora, e a todos os outros que não cito por aqui. Obrigado, mesmo! Agradeço ao Dr. Bruno Martins por sempre ter me aconselhado e me ajudado com relação as especificidades técnicas referentes à microscopia de tunelamento.

I sincerely thank all the people that helped during my period in Basel. Among them, I would like to specially thank Aneliia Shchyrba – your willingness to work together with me has made all the difference. I also thank Sylwia and Thomas Nijs, the environment in the lab was really cooperative and friendly. Professor Thomas Jung should also be mentioned: he accepted to host me in Basel and also provided me with the necessary elements towards producing exciting science. I acknowledge him for the opportunities that yielded from my stay in Basel.

À FAPESP pelo apoio financeiro (bolsa regular 2012/16860-6 e bolsa BEPE 2013/04855-0) e ao CNPq.

Por ultimo, mas um dos pilares mais importantes, gostaria de agradecer minha mãe e nona por sempre estarem ao meu lado em minhas decisões. O zelo de vocês para comigo é inestimável.

“The Road not taken

Two roads diverged in a yellow wood,
And sorry I could not travel both
And be one traveler, long I stood
And looked down one as far as I could
To where it bent in the undergrowth;
Then took the other, as just as fair,
And having perhaps the better claim,
Because it was grassy and wanted wear;
Though as for that the passing there
Had worn them really about the same,
And both that morning equally lay
In leaves no step had trodden back.
Oh, I kept the first for another day!
Yet knowing how way leads on to way,
I doubted if I should ever come back.
I shall be telling this with a sigh
Somewhere ages and ages hence:
Two roads diverged in a wood, and I –
I took the one less traveled by,
And that has made all the difference.”

ABBREVIATION LIST

STM	Scanning Tunneling Microscopy
STS	Scanning Tunneling Spectroscopy
I(z)	Current-distance Spectroscopy
XPS	X-Ray Photoelectron Spectroscopy
TPP	Tetraphenyl Porphyrins
NiTPP	Nickel Tetraphenyl Porphyrins
Pc	Phthalocyanines
CuPc	Copper-Phthalocyanine
MnPc	Manganese-Phthalocyanines
SCA	Single Component Assemblies
BCA	Bi-component Co-assemblies
LEED	Low energy electron diffraction
HOMO	Highest occupied molecular orbital
LUMO	Lowest unoccupied molecular orbital

1 INTRODUCTION

The famous, and widely spread, speech of Richard Feynman in 1961 [1] reflects on the inexistence of limiting nature laws that would prevent mankind to perform the control of atoms and molecules, one of the components in the quest towards mimicking nature. But Feynman also pointed out that at that time no standard technique was able to execute such task. The Scanning Tunneling Microscope (STM), developed in 1981 at IBM R schlikon [2], opened up a systematic way for the observation of matter in the nanoscale in real space (one has to note that atoms had already been resolved in a specific case via Transmission Electron Microscopy [3]).

It took nearly eight years so that besides observing atoms and molecules it was possible to manipulate them, with the work of Donald Eigler, when Xe atoms were manipulated on top of a Ni(111) surface using the STM [4]. Nowadays, the manipulation procedure is still far from being trivial, being a time consuming task and requiring expensive equipment. Nevertheless, progress has been made, with the recent manipulation of five hundreds CO molecules, in molecular cascades [5]. Unfortunately, such constructions are not easily reproducible.

The National Nanotechnology Initiative, initiated by the US Government, has detected that until now (02/2014) no large scale nanomanufacturing of devices has been obtained [6]. One of the reasons for this is that the scalability of nanoscale experiments is far from being trivial. In order to overcome the experimental issues it is necessary to properly address fundamental aspects of matter at the nanometer level, such as structural and electronic properties, which are different than its bulk counter-part. It is also necessary to devise different routes to create nanostructured systems.

There are basically two routes by which nanosystems can be constructed: the top-down and the bottom-up approaches. The top-down approach consists in starting with bulk materials and through some physical modification one obtains elements in the nanoscale or nanostructured materials, with an example of technique being the lithography [7]. One practical example of the top-down approach, and that has been extensively treated in literature, is the obtainment of a graphene sheet by using scotch-tape and bulk graphite [7]. Problems with the top-down approach are with selecting proper crystallographic orientations of nanosystems and the extensive existence of defects in large scale.

The second route for obtaining nanoscaled systems is the bottom-up approach. It consists of starting the process with nanoscale entities, e.g. atoms and molecules. Through physical transformations, these entities can bind to each other in specific ways and create the final structure. Examples of the bottom-up approach are the manipulation with the STM, chemical synthesis and the self-assembly. The later will be explored throughout this dissertation.

The self-assembling technique has been explored since the end of the 90's [8]. This technique is interesting because it enables the creation of ordered nanosystems in a quick and low cost fashion. The self-assembling process occurs when the entities of the system (molecules in this thesis, for example) interact both with other entities and also with the medium (the surface in this thesis, for example). In order to minimize the energy of the system, these entities end up forming bigger and more complex structures which can be ordered.

Better understanding of self-assembling properties provides the necessary elements for the development of nanostructured devices. For example, molecular devices have been manufactured via self-assembling routes, such as gas sensors [9]. Lately, 2D self-assembled supramolecular systems have received increased attention. Several systems have been studied, resulting in the development of different devices: molecular gas sensors [10], new catalysts [11] and molecular thin films mimicking electric components [12]. Yet, we are still far from producing such devices in large scale. The basis for all the exemplified devices are the use of molecular thin films grown on top of metal surfaces, the topic of this thesis.

In that sense, we are interested in the properties of molecular self-assembled thin films on top of metallic substrates. This thesis is based on the use of planar aromatic molecules and their self-assembly on metallic substrates. First (chapter 2), we discuss the experimental techniques used in this thesis: Scanning Tunneling Microscopy (STM) and X-Ray Photoelectron Spectroscopy (XPS). Both techniques are well-suited for the study of the molecular self-assembly process because they supply fundamental information towards structural and spectroscopic understanding of how molecules interact forming different patterns. On the other hand, these techniques do not damage the analyzed samples: the highly local electric fields (of the order of 10^8 V/m) are applied for brief periods of time (of the order of 0.1 s) in the case of STM and the intensity of the utilized x-rays (emitted from a regular Al or Mg source) are not sufficient to fragment the molecules. In Chapter 3 we address the self-assembly properties of Nickel-Tetraphenyl Porphyrins on Cu(111) and vicinal gold substrates. The goal of this work, performed in Brazil, was to gain

know-how on molecular systems, an area away from the mainstream surface science studies and from the previous researches of the group in Campinas. Finally, in Chapter 4, we study another aromatic molecule – phthalocyanine – on different metallic substrates towards the goal of producing a chessboard bimolecular array that could be used in gas sensor probes. This part of the work was performed at the Nanolab group of Prof. Thomas Andreas Jung in the Department of Physics of the University of Basel (Switzerland)

2 EXPERIMENTAL METHODS

This chapter introduces the theoretical background for the experimental techniques utilized on this thesis. In more details, we explain both the Scanning Tunneling Microscopy (STM) and X-Ray Photoelectron Spectroscopy (XPS). Apart from the major techniques, molecular epitaxy is also explained in general terms.

2.1 SCANNING TUNNELING MICROSCOPY

The invention of the STM in 1981 by G. Binnig, H. Rohrer and Ch. Gerber opened a plethora of possibilities of new studies for the analysis of surfaces. This technique proved to be robust by resolving atoms on a metallic substrate [2] and also settling the debate over the (7×7) -Si(111) reconstruction by using its images in real space [13].

Moreover, this technique provided a solid background in terms of its working principle and signal processing. These characteristics led to the invention of several others methods that employ similar mechanisms while measuring different physical quantities, from forces to specific heat [14].

The mechanisms for which the above mentioned techniques are based utilize a probe that sense different physical properties of surfaces while scanning predetermined points in a grid. Therefore, such techniques derived from the STM are denominated Scanning Probe Microscopies.

This section explains the physical principle of the STM, including also the I-z spectroscopy, scanning tunneling spectroscopy (STS) and the molecular resolution of the STM.

2.1.1 Physical Principle

The physical phenomenon employed by the STM technique is, as pointed out in its name, the tunneling effect. To that extent, a current is measured between a tip and a sample. Classically, if a confined particle do not possess energy higher than the energy barrier of the system, then

it is not possible to find such a particle on outer region limit. In terms of the formalism of the quantum mechanics, the problem has a different result. Consider the potential barrier problem of width d , treated in any quantum mechanics text book. The probability of finding a particle of mass m in the outer region of the barrier using the Schrödinger formalism is equals to e^{-2kd} , where $k = \frac{\sqrt{2m(V-E)}}{\hbar}$, \hbar for Planck's constant, V is the energy barrier of the potential and E for the energy of the particle.

Experimentally, this phenomenon is probed utilizing a sharp metallic tip and a conducting substrate. Initially both objects have their own work functions, respectively ϕ_{Tip} and ϕ_{Sub} depicted in Figure 1 A and are apart. By connecting them, their Fermi levels align, and this creates in the vacuum region an asymmetric barrier for electrons from both sides (Figure 1 B). After the two electrodes reach the electric equilibrium, it is possible to apply between them a voltage V . This results in a gap between the Fermi levels of the electrodes which is equal to eV (Figure 1 C).

The apparent barrier height for an electron can be written as the average between the work functions of the two electrodes. Then, the tunneling current measured at the tip is proportional to the probability of acquiring electrons that arise from an energy ranging from the Fermi level to the Fermi level minus eV . This yields the same mathematical expression shown for the transmission probability of finding an electron, equals to e^{-2kd} , with $k = \frac{\sqrt{2m_e\phi_{average}}}{\hbar}$.

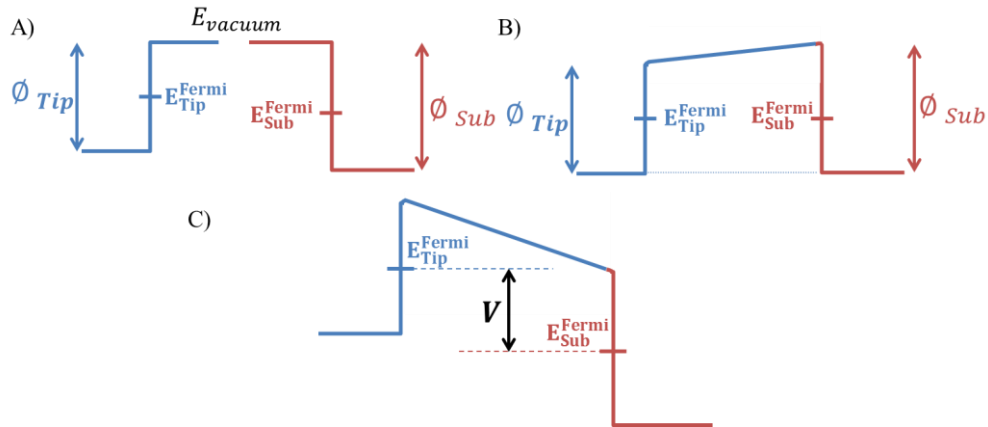


Figure 1: Energetics change of vacuum barrier for two electrodes (tip and substrate). A) Tip and sample not connected. B) Tip and sample in electric equilibrium. C) Tip and sample with an energy barrier between Fermi levels of eV .

This simple relation explains the high vertical resolution of the STM technique. If one utilizes an average value of 4-5 eV for the work function of both the tip and sample, increasing the distance d between tip and sample of the order of two atom's diameter yields a two order of magnitude decrease in the measured current.

Another important facet of the STM, as pointed out by Tersoff [14] is the lateral resolution of the tip. If one considers a parabolic terminated tip with radius R , at a certain lateral distance x with respect to the center of the tip in a one dimensional model, the current is proportional to $e^{-K\frac{x^2}{R}}$. This yields a Gaussian profile of the current, with a root mean square lateral distance measurement of approximately $0.7\left(\frac{R}{K}\right)^{\frac{1}{2}}$. Considering the average radius of low-cost microscopes in the 100 Å range, which can be considered equal to 40 tungsten atoms in a row, and a typical K of 1 Å^{-1} , this provides a lateral resolution of 28 Å. So even with a rather badly conditioned tip it is possible to obtain a sharper resolution in the range of few nanometers, but not atomic resolution. Experimentally, what is known to occur is that it is needed to condition the tip using voltage discharges or crashing the tip several times so that at its termination it possesses few atoms, which would result in high resolution, i.e. atomic resolution [15].

In a more formal setting, as performed by Bardeen [14], the tunneling current can be written in terms of the density of states of both tip and sample. The importance of analyzing this problem is the concept of local density of states per energy interval in a specific position, defined as

$$\rho(\vec{r}, E) = \sum_{\nu} |\psi_{\nu}(\vec{r})|^2 \delta(E_{\nu} - E) \quad (1)$$

Using Fermi's golden rule, it is possible to write the number of electrons flowing from tip to sample in terms of the density of states of the tip and sample modulated by the probability of an occupied state, via tunneling, to occupy an unoccupied state, given by Fermi's distribution. The calculation yields [16]:

$$I_{tip \rightarrow sample} = \frac{2\pi e}{\hbar} \int_{-\infty}^{\infty} \rho_T(\epsilon - eV) f(\epsilon - eV) \rho_S(\epsilon) [1 - f(\epsilon)] |M_{T,S}|^2 d\epsilon \quad (2)$$

where $f(\epsilon) = \left\{1 + \exp\left[\frac{(\epsilon - \epsilon_F)}{k_B T}\right]\right\}^{-1}$ is Fermi's distribution, e is the electron charge, \hbar Planck's constant and $M_{T,S}$ is the tunneling matrix which amounts to a surface integral correlating the states of the tip and sample and its coupling. An analog expression can be written for the current flowing from sample to tip:

$$I_{sample \rightarrow tip} = \frac{2\pi e}{\hbar} \int_{-\infty}^{\infty} \rho_T(\epsilon - eV)[1 - f(\epsilon - eV)]\rho_S(\epsilon)f(\epsilon)|M_{T,S}|^2 d\epsilon \quad (3)$$

The net current, then, can be written:

$$I = \frac{2\pi e}{\hbar} \int_{-\infty}^{\infty} \rho_T(\epsilon - eV)\rho_S(\epsilon)[f(\epsilon - eV) - f(\epsilon)]|M_{T,S}|^2 d\epsilon \quad (4)$$

Experimentally it is difficult to determine the tunneling matrix in a more realistic framework. But since the tip geometry affects both the density of states and the wave functions interaction towards the sample, it is necessary to understand it more systematically and to obtain a clear physical impression about what is the meaning of the tunneling current. In the approximation made by Tersoff and Hamann [16] first order perturbation theory is applied to a system whose tip interaction consists of a single atom on its apex. By stating that, only the last atom of the tip at the apex should be considered in the tunneling regime, and only the s-orbital should interact with the sample. At low bias V

and low temperature the tunneling current can be written as

$$I = \frac{4\pi e}{\hbar} \rho_T \int_0^{eV} \rho_S(\epsilon) |M|^2 d\epsilon \quad (5).$$

Physically this means that the tunneling current, in a simplified form, is proportional to the electronic charge density of the sample. But unfortunately, such a widely propagated model, as stated by Chen [15], only correctly explains some of the topographic measurements of STM, as it fails to describe the atomic corrugation of low index metal surfaces. One of the main problems with this and all the subsequent approaches is the fact that the main entity in the STM measurement, the tip, is not known prior to the measurement itself and it can also change during the measurement. More complex approaches, for example, considering a p - or d - like orbital of the tip also possess more mathematical complexity and if not entirely, emulate certain aspects of the topography obtained nowadays in scanning probe techniques [17].

Operationally, the microscope has an approaching mechanism based on piezoelectric actuators (piezos). By applying a voltage on the piezos we can either move the tip or sample in Cartesian coordinates. The tip acquires the tunneling current, which passes through an amplifier so it can be processed. After amplifying the current, it is compared in a feedback loop, which can either be controlled to maintain the tip-sample distance constant while moving throughout the scan frame (constant height mode) or it can move the z-piezo (which defines tip-sample height) until a predefined current is reached (constant current mode). The constant height mode is usually quicker, since no comparison to a set point current is needed. But on the other hand, if the sample

area is irregular, with several height differences, this might crash the tip. All measurements performed in this dissertation were in the constant current mode.

2.1.2 Scanning tunneling spectroscopy

Besides the ability to scan areas and to picture the density of states in the surface, one of the most powerful tools of the STM is its capability to perform spectroscopy. Since some of the results presented in this Master dissertation use the results obtained from Scanning Tunneling Spectroscopy (STS), it follows the description of the technique and its physical interpretation.

Assuming that the calculated net tunneling current has a tunneling matrix that does not depend on the energy at which one probes the tip/sample system, which physically means that there is no difference in the correlation and in the coupling between tip and sample for different samples, the current can be written as:

$$I \propto \int_{-\infty}^{\infty} \rho_T(\epsilon - eV_T) \rho_S(\epsilon) [f(\epsilon - eV_T) - f(\epsilon)] d\epsilon. \quad (6)$$

Where V_T is the bias voltage applied between tip and samples. Differentiating with respect to V_T and considering that the density of states of the tip is kept constant during the measurement ($\rho_T' = 0$) yields:

$$\frac{\partial I}{\partial V_T} \propto -\rho_T \int_{-\infty}^{\infty} \rho_S(\epsilon) f'(\epsilon - eV_T) d\epsilon. \quad (7)$$

Considering that the STS is performed at low temperatures, since only with such setting is possible to reach acceptable energy resolution (later discussed), one can approximate the derivative of the Fermi's distribution to a Dirac's delta function ($f'(\epsilon - eV)_{T \rightarrow 0} = -\delta(\epsilon - eV)$). So finally the derivative of the tunneling current is

$$\frac{\partial I}{\partial V_T} \propto \rho_T \int_{-\infty}^{\infty} \rho_S(\epsilon) \delta(\epsilon - eV_T) d\epsilon = \rho_T \rho_S(eV_T). \quad (8)$$

This means that by measuring the tunneling current behavior with respect to the variation of the applied bias voltage results in a fingerprint of the local density of states of the sample.

Technically, the tunneling current is noisy and this would not enable correct measurements of dI/dV due to the fact that the background signal would be, in some cases, of the same order of the spectrum measured. To solve such issue, one uses a modulation in the applied bias voltage. By expanding the tunneling current $I(V + V_{mod} \cos(\omega t + \varphi_0))$ at the bias voltage V_T :

$$I_{V_T} = I(V_T) + \frac{dI}{dV_{V_T}} V_{mod} \cos(\omega t + \varphi_0) + \frac{d^2I}{dV^2_{V_T}} V_{mod}^2 \cos^2(\omega t + \varphi_0) + \dots \quad (9)$$

where φ_0 is the signal modulation phase. By measuring the signal variation along the frequency used, it is possible to obtain the derivative signal with high accuracy. To execute such modulation a Lock-In amplifier is used. It is used to modulate the signal and also to collect the resulting modulation in tunneling current. It also filters signals which have a different frequency ω and phase φ_0 .

In order to use STS, it is necessary to keep in mind that, besides the instrumental resolution due to the phase determination of the Lock-In [18], the temperature at which the experiment is performed also influences the energy resolution. The energy resolution ΔE is given by the thermal energy and also by the voltage modulation which is used, in the following relation $\Delta E = \sqrt{(3k_B T)^2 + (2.5eV_{mod})^2}$, where k_B is Boltzmann constant, e is the charge of the electron and T is temperature of tip-sample. The first term comes from the minimum necessary resolution to separate two delta-like energy peaks. The second term comes from the experimental resolution of the equipment, when a sharp signal in energy is measured and convoluted with the voltage modulation. This results in a broadening of approximately $2.5eV_{mod}$ [19]. As an example, performing STS with the following parameters $T=4K$ and $V_{mod} = 8$ mV, yields an energy resolution of approximately 20 meV. Throughout all of our measurements, the frequency utilized was 512 Hz and the modulation voltage was 8 mV.

2.1.3 I(z) spectroscopy

Besides obtaining topographs and spectroscopically probing the density of states of the sample, STM can also be used as a local tool to evaluate the relative work functions of nanostructured systems. Using the same formalism as the Tersoff-Hamann model, $I = \frac{4\pi e}{\hbar} \rho_T \int_0^{eV_T} \rho_S(\epsilon) |M|^2 d\epsilon$. For an over simplified situation at which the density of states of the sample is also kept constant and the tunneling matrix is written using a 1-D simplification of a trapezoidal barrier, the tunneling current is proportional to

$$I \propto V_T e^{-2\sqrt{\frac{2m\phi}{\hbar^2}}z}, \quad (10)$$

where z is the tip-sample distance and ϕ is the averaged work function between sample and tip. Therefore, if we measure the tunneling current as a function of tip-sample distance, it is possible to obtain the value of ϕ . This assumption is true under all simplified conditions that we have used so far, i.e., low temperature, bias voltages and also tip-distance displacements.

In order to ensure that such conditions are satisfied, all our $I(z)$ measurements were performed with currents of 100 pA, a sample bias of 1V and a displacement of the tip of the order of 0.5 Å.

2.1.4 Molecular imaging with the STM

Since the development of STM, it was expected that molecules were invisible for its measurement. The reason was that STM probes the density of states near the Fermi level and the molecules present a gap between the highest occupied molecular orbital (HOMO) and the lowest unoccupied molecular orbital (LUMO) and in known molecules the gap was of the order of few electron volts.

However, after the first experiments trials with planar molecules such as phtalocyanines on Cu(100) [19], it became clear that the hybridization between molecule-substrate states produces a shift of the energy levels making it possible to image the hybridization orbitals, which resemble for some conditions the physical appearance of the molecules.

2.2 X-RAY PHOTOELECTRON SPECTROSCOPY

Although Scanning Tunneling Microscopy is a very important technique for obtaining real space information about the surface, it is very difficult to obtain chemical element sensitivity and, even on extraordinary cases, the chemical resolution is obtained for very limited areas (of the order of hundreds of nm²) [21]. Contrastingly, the X-Ray Photoelectron Spectroscopy (XPS) offers complementary information to the one obtained via STM. XPS is a technique that detects different elements and enables quantification of elements concentration and also the identification of their chemical state.

XPS, was invented by Kai Siegbahn [22] and is routinely applied in laboratories throughout the world in order to probe the surface composition of different samples. We present a view of the physical and operating principles of XPS.

2.2.1 Physical principles

XPS is based on the photoelectric effect (discovered by Hertz in 1887). On this technique, X-ray photons interact with the electrons of a solid (Figure 2 A). This interaction occurs with the core-level or valence electrons of all atoms of a solid and is depicted in Figure 2 B. By conservation of energy we obtain that E_K , the kinetic energy of the electron removed from the core-shell, can be expressed as

$$E_K = h\nu - \phi - E_B, \quad (11)$$

where $h\nu$ is the x-ray photon energy, ϕ the material's work function (which is the energy between the vacuum and the Fermi level of the material), and E_B is the binding energy of such electron. Since the binding energy is different on the energetic level of the electron and varies according to the atomic species, it is possible to observe that the measurement of the electron kinetic energy is related to the chemical specificity of different elements in the sample.

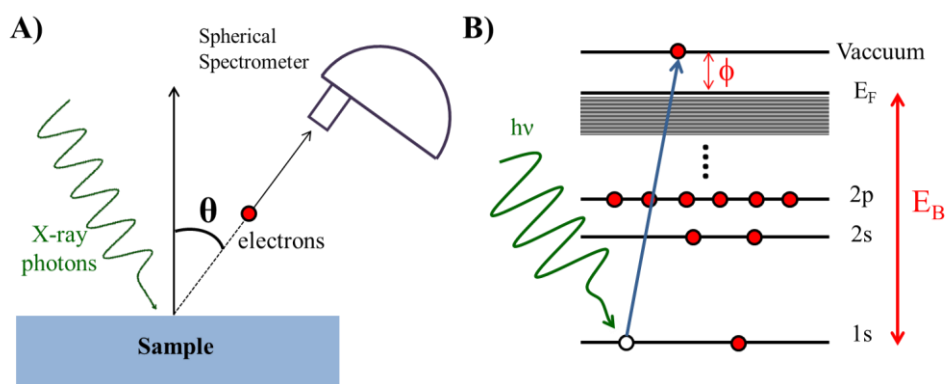


Figure 2: XPS schematics. A) Experimental arrangement of the XPS experiment, where X-ray photons are directed to a sample and electrons that have interacted with the electromagnetic wave are collected in the spherical spectrometer. B) The emission process, where photons interact with core-level electrons that surpass the energetics of the binding energy E_B and the work function ϕ , keeping a kinetic energy E_K .

After the electron has been ejected with energy E_K , the electrons are collected in a spectrometer. By electrically connecting the spectrometer to the sample, it removes the work function ϕ of the sample and adds the work function of the spectrometer $\phi_{spectrometer}$, which is obtained experimentally. The collected electrons with varying kinetic energies experience an electric field due to the different electrical potentials applied on the outer and inner shell of the spherical spectrometer. This enables us to probe specific energies to be collected, ranging from close to zero up to the photon energy. In fact, the cutoff energy can be used to precisely measure the ϕ_{sample} .

A regular XPS measurement acquires the intensity of electrons at a certain binding energy E_B , for binding energies ranging from the photon energy to zero. The peaks observed have a non-null width which is a convolution of the width contribution in energy of the photon source, the lifetime of the excited state and the resolution of the analyzer on the spectrometer.

As mentioned before, XPS is known to be a surface sensitive technique even though x-rays interact with the sample in depths of the order of micrometers. But in the energy range at which we work with (Al or Mg K_α – 1486.6 or 1253.5 eV, respectively) the inelastic mean free path (IMFP) of the produced photoelectron is of the order of 30 Å in a copper sample, as shown in Figure 3 (data taken from literature [23]). Therefore, most (~66%) of the electrons detected in the spectrometer comes from up to 30 Å below the surface.

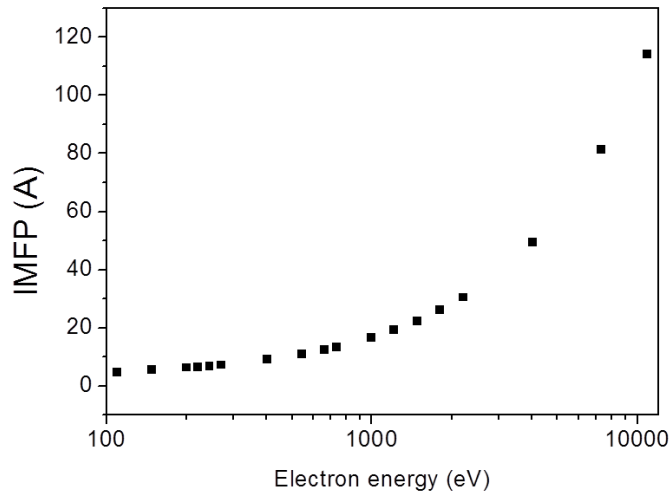


Figure 3: Inelastic mean free path of electrons in function of their kinetic energy on a copper sample. Taken from [23].

By changing the angle θ between the normal vector of the sample and the spectrometer (Figure 2 A), it is possible to tune the depth analyzed. The XPS intensity signal of a thin film is proportional to $[1 - \exp(-\frac{d}{\lambda(E_C)\cos\theta})]$, where d stands for the thickness of the thin film and $\lambda(E_C)$ is the inelastic mean free path of the electron with the kinetic energy at which it is analyzed. For layer-by-layer film growth, angle resolved XPS (ARXPS) is typically used to determine the film thickness.

It is also possible with XPS to quantify the concentration of elements. In order to obtain such values, it is necessary to calculate the area of the peaks of all the elements (A_α) and normalize it with the sensibility factor (S_α) [24], where α corresponds to all elements of the thin film analyzed. Then, the concentration of element A can be expressed as

$$C_A = \frac{\left(\frac{A_A}{S_A}\right)}{\sum \alpha \left(\frac{A_\alpha}{S_\alpha}\right)}. \quad (12)$$

In all XPS measurements of this thesis, to verify that molecules were correctly sublimated we determined the concentrations of the elements.

2.2.2 Chemical Shift

Besides obtaining element specificity in the XPS measurements, it is possible to obtain the chemical state of an element as well. The binding energy is not only a measurement of the energetic level at which photoemission is occurring but also reflects the organization of the valence band. Using a hollow conductive sphere as analogy, the electrostatic potential is proportional to the charges on the surface, if the charges in the sphere change, the potential changes with the same sign. The physical meaning of the variation of electrostatic potential is the change on the binding energy. This is the reason why it is possible to discern between different oxidation states and also between different bonding of the same element [24].

2.3 MOLECULAR EPITAXY

In order to study the self-assembling properties of molecules, it is necessary to deposit them properly on a clean substrate. To that extent, we have used the physical process of thermal sublimation. This mechanism consists of providing thermal energy to the volume where the desired evaporating material is maintained, this thermal energy is transformed into kinetic translational energy of the evaporant.

Technically it consists of a Knudsen cell [25], which in our case was a quartz crucible rolled on the outside by a metallic wire, which acts as a resistance and dissipates power. This power produces heat in the wire, which is transferred to the region of crucible by irradiation and, depending of the contact points to the quartz crucible, conduction. The conversion between thermal to kinetic energy results in molecules being ejected from the crucible in all directions. By creating one direction oriented opening on the crucible, only the molecules directed towards a preferential direction are allowed to be ejected.

Concerning the molecules, it is necessary to outgass them in the same manner as one outgasses the chamber. Due to contamination of the chosen molecular powder or even contamination from the crucible, it is necessary to thoroughly outgass for long periods of time. Empirically we noted that an optimal condition to prepare the evaporator is to degass the molecules for 12 hours at a power slightly lower than the one at which molecules start to depart from the crucible. After this procedure, we then reach the temperature at which there is a rise in the pressure of the chamber, and one expects molecules to start leaving the crucible, and depositing on a clean substrate placed in front of the crucible. By analyzing such modified substrate with XPS, it is possible to infer the ratio between the different constituents of the molecule and compare to the stoichiometry values of the molecules. If these two values do not match, the temperature should be increased and the same procedure repeated again, this time with a higher power.

Another important procedure is to observe at which temperature the molecule starts to decompose. It is the temperature for which the energy is sufficient enough to break the covalent bonds within the molecule being used. Usually in molecules that possesses up to 10 atoms, the decomposition temperature ranges closely to the temperature of evaporation. This is one of the reasons for the development of other molecular deposition methods, for example, electrospray ion beam deposition.

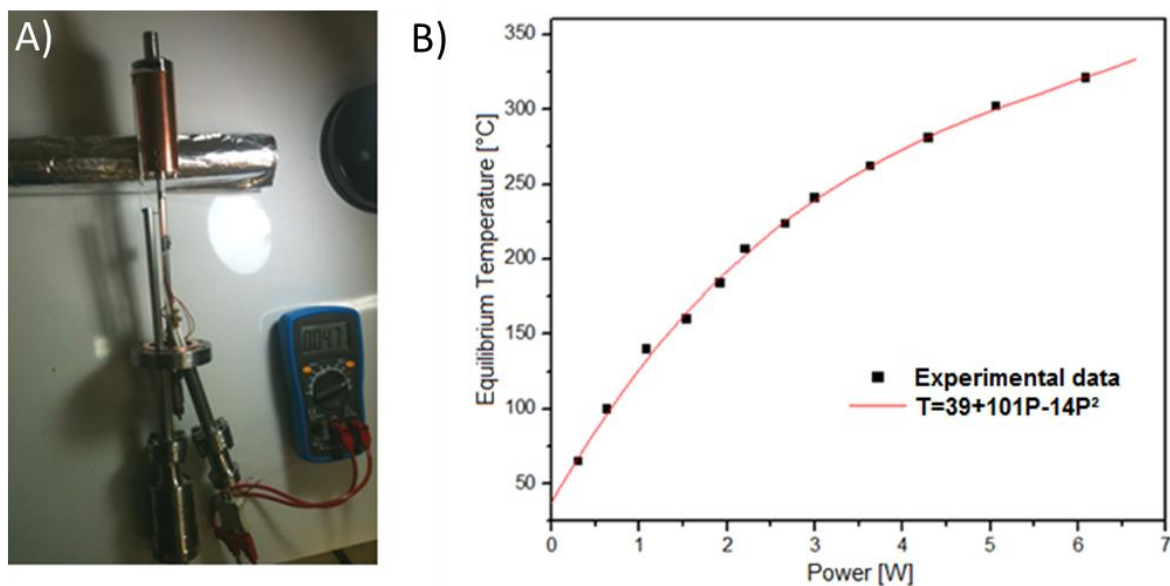


Figure 4: Knudsen cell utilized for this work. A) Experimental apparatus. B) Measurement of the equilibrium temperature inside the crucible of the cell versus the power utilized.

The experimental apparatus used for the deposition of NiTPP is shown in Figure A. In order to correctly deposit the molecules, we can use as a measure for deposition both the power inserted in the wire and the temperature measured inside in the outer part of the crucible by a thermocouple. For the case where the thermocouple is broken inside the UHV environment, we have fitted a polynomial relation between the applied power to the metal wire and the equilibrium temperature obtained, as attested in Figure B.

3 NICKEL TETRAPHENYL PORPHYRINS ON LOW INDEX AND VICINAL METAL SURFACES

This chapter discusses the studies involving the adsorption of NiTPP on low index surfaces, Cu(111), and vicinal surfaces, Au(332) and Au(788). This research was performed within the facilities of the Surface Science Group of the Applied Physics Department at the University of Campinas. All experiments performed in this chapter were done at room temperature. At first, we discuss the importance of tackling the problems and control of molecules on metal substrates. Next, the analysis of NiTPP/Cu(111) is presented followed by NiTPP/Au(332) and NiTPP/Au(788).

3.1 INTRODUCTION

The study of molecular systems on metallic substrates ranges from the fundamental understanding of different bonding mechanisms of molecules [26] to how it relates to different nano patterns on the surface [27]. Such understanding enhances not only the ability to extend our control over nature, but also envisage future applications which might be thought of.

In the sense of controlling the formation of different self-assembled nanostructures, our goal is to start in the area of molecular nanoscience at the Surface Science Group but also seeking for a system which was not treated in literature so one could grasp the recent results of the field and try to follow through our own path. In such sense we decided to use a commercial molecule. This would enable the research to initiate in a timeless fashion in contrast to contacting a chemist and requiring the synthesis of a new molecule.

Recently, in literature, it was shown the possibility to explore the structural properties of CoTPP allied with the possibility to turn the magnetism ON/OFF depending on the chemical species adsorbed on top of CoTPP [28]. Since the group is interested in future use of molecular arrays to probe magnetism, we decided to use molecules of the tetraphenyl porphyrin family. Thus, the chosen molecule was NiTPP. The goal was to understand its structural properties in a low index substrate at which it had never been reported in literature, Cu(111) and then advance to

vicinal surfaces in order to observe the differences that constraining the terraces would force on the self-assembling process and whether control on the growth of molecules was possible.

3.2 NICKEL TETRAPHENYL PORPHYRINS

Tetraphenyl porphyrins are molecules of the class of the porphyrins, which possess two pyrrole groups covalently bonded to a methine group ($-C=$) forming a part of the macrocycle, represented in Figure 5 A. Each phenyl bonds to a methine group, as well. The porphyrin molecules are aromatic, which means that they possess a ring with p-orbitals on the carbon atoms and delocalized electrons throughout the ring. Aromaticity is important because it means that the macrocycle possess mechanical stability and does not decompose while interacting with other atomic elements. Instead of possessing two hydrogens on each amine group ($-NH-$), these hydrogens can be desorbed and create a binding site for an atom to be inserted in the center of the macrocycle. This ion is coordinated to four pyrrole nitrogens, which leaves the ion in a $[ion]^{+2}$ state and the macrocycle with a D_{4h} symmetry [29]. Examples of atoms that are allowed as centers of the macrocycle are the transition metals.

Porphyrins are a very important class of molecules in nature. One can cite the *heme* group of hemoglobin that contains a porphyrin with a Fe center. Depending on the conformation of the porphyrin macrocycle, the Fe center can act as a binding site to oxygen [30]. Another important porphyrin in nature is chlorophyll, which possesses a Mg center, and plays a fundamental role on photosynthesis.

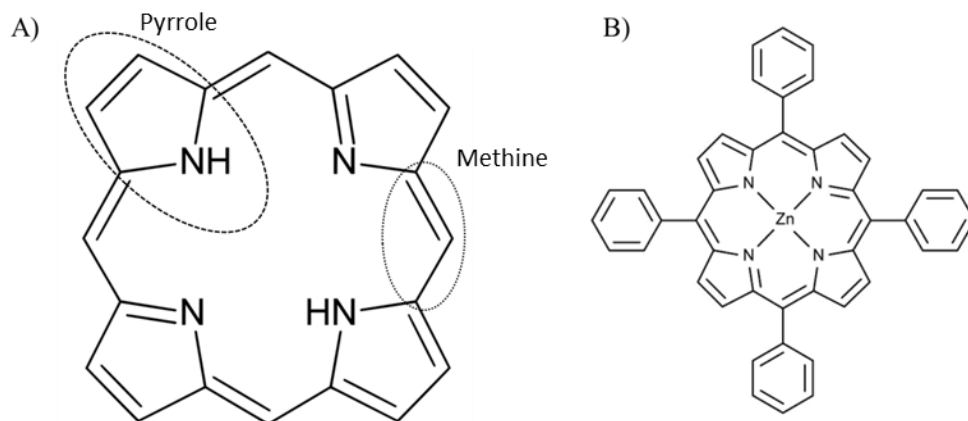


Figure 5: Tetraphenyl porphyrin scheme A) Macrocycle of a tetraphenyl porphyrin, composed of four pyrroles connect by a methine carbon. B) At each methine a phenyl ring is connected. On its cavity the TPP has a Zn atom as well.

However, natural porphyrins as those cited above are challenging to synthesize and possess several degrees of freedom, due to their molecular size composed of more than 60 atoms (excluding hydrogens). The size of natural porphyrins allows for complex and diverse conformations. Technically, only a few set of high spatial resolution techniques allow the exact position of all molecules constituents to be probed such as high-resolution atomic force microscopy [31].

On this sense, tetraphenyl porphyrins (TPP) although complex, offer fewer challenges to their analysis than natural porphyrins. TPP possesses a porphyrinic macrocycle and phenyl rings connected to the methine carbons of the macrocycle. So, in terms of degrees of freedom, the molecule can have the phenyl rings being rotated and bending of the macrocycle, depending on the interaction to the substrate. This makes TPP a good prototype of natural porphyrins for adsorption studies on surfaces. It is also possible to have TPP with metal ions in the center of the macrocycle, depicted in Figure 5 B. This type of TPP is named metal tetraphenyl porphyrin. Some of these molecules present interesting magnetic properties. CoTPP, for example, is able to couple with NO while adsorbed on a surface and act as a magnetic switch [28]. Here, NO donates an electron to the cobalt center of the molecule and transforms the d_{z^2} of CoTPP in a hybridized filled orbital. When the substrate is heated, the NO is desorbed from the molecule, and the CoTPP returns to its magnetic state.

The molecules utilized throughout this chapter are the NiTPP. They were chosen for two reasons: the interesting magnetic character of the Ni on the molecule, which may be used in future magnetic experiments of the group, is necessary to obtain a thorough understanding of how

these molecules adsorb on different substrates, ranging from the commonly used basal to the vicinal substrates. In this case, understanding different coverage adsorption plays a decisive role on eventual possible experiments involving magnetism. Another reason for choosing NiTPP is that contrary to the several reports in literature concerning CoTPP and TPP's, NiTPP's adsorption properties were less known by the time the work was performed and still offered some challenges in when deposited in higher reactive surfaces as, for example, Cu(111).

3.3 NITPP ON CU(111)

3.3.1 Cu(111) surface

The first substrate utilized is a low index copper crystal. It was bought from Monocrystals Inc. USA and stated to have less than an 0.5° error in the desired direction. Copper is a face cubic centered crystal and in the (111) direction we obtain a hexagonal close-packing structure.

Prior to molecular deposition, we have extensively cleaned the substrate by cycles of Ar^+ sputtering (1.5 kV, $1.3 \mu\text{A}/\text{cm}^2$) and annealing at 800 K. XPS and STM were employed to check sample cleanliness and the formation of large terraces.

3.3.2 One dimensional molecular adsorption

In the NiTPP/Cu(111) system, for submonolayer coverage (0.1 ML) we observed that NiTPP molecules anchor in the step edges of the substrate. The STM images of submonolayer coverages of NiTPP on Cu(111), taken at room temperature, are summarized in Figure 6 A. The rounded spots represent the molecules deposited in the substrate. NiTPP has such appearance because of the low resolution of the microscope for this image size ($54 \times 37 \text{ nm}^2$).

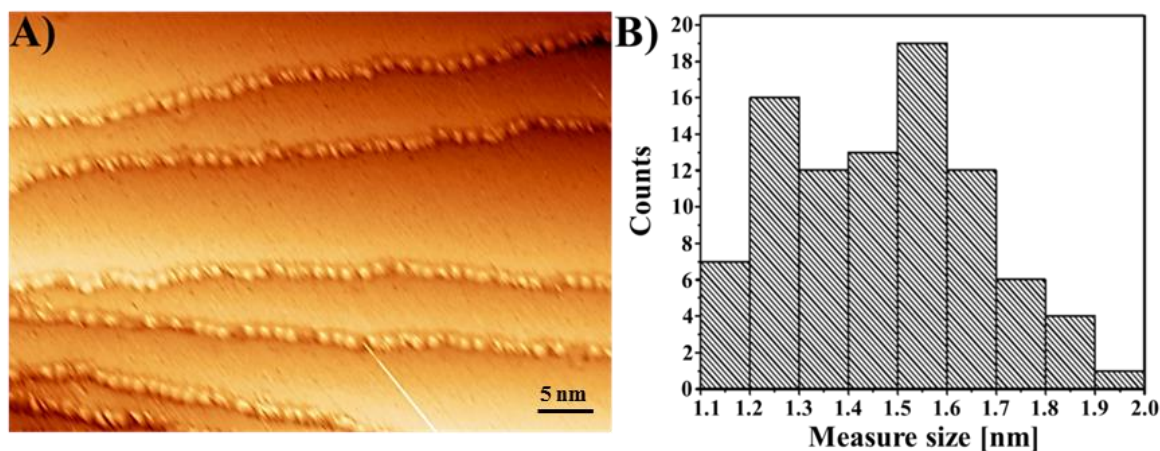


Figure 6: A) STM image ($54 \times 37 \text{ nm}^2$) of NiTPP wire formation along the step edges of Cu(111). Bias voltage was 1.2 V and the tunnelling current 0.5 nA. The coverage was lower than 0.1 ML. B) Measurements of molecules on the step edges. The histogram of the measured lateral size of the molecules throughout the step edges, indicate that molecules are displaced in a disordered manner.

By measuring the parallel length of the molecules along the step edge, it was possible to relate such size with the angle to which the molecule is oriented across the step edge. We note from Figure 6 B that the size distribution is random. Throughout the frequency of measured sizes, we observed a maximum fluctuation of 9 counts related to the sample average of 10 counts. The maximum deviance accepted for a uniform distribution composed of 90 measurements is 9.4 [32] so we conclude that our distribution of size can be assumed as uniform.

Although the molecule size should vary from 1.2 to 1.8 nm in the histogram in Figure 6 B it is also possible to see measurements lower than 1.2 nm and greater than 1.8 nm. This is explained by the argument that some molecules might be superimposed in the images and some molecules might have been camouflaged with step edges defects.

Whenever elements such as carbon, sulphur or oxygen are present in a metallic surface, they tailor the properties of the step edges of the substrate and serve as anchors for the molecules but XPS measurements confirmed the cleanliness of the copper surface.

Our proposed explanation is that due to high reactivity between the Cu(111) step edge and the NiTPP, in submonolayer regime of 0.1 ML, the step edges act as a trapping potential with a barrier energy higher than the energy associated with room temperature. These results differ from the one obtained by Rojas et al [33] on the $\text{H}_2\text{TPP}/\text{Cu}(111)$ system when in low coverage the H_2TPP do not present step decoration. Different metallic tetraphenyl porphyrins such as CoTPP also show step decoration on metallic substrates such as Au(111) and Ag(111) [34].

At coverage lower than 0.1 ML, NiTPP formed also a mobile phase at room temperature, which was evident by the streaky features in STM images.

3.3.3 Transition between disordered one-dimensional and ordered two dimensional adsorption

The behavior of NiTPP towards 2D nucleation was also analyzed in our experiments. During the transition between 0.1 ML and 1.0 ML the nucleation of the NiTPP was found to start at the step edge. No free-islands of NiTPP were observed on the Cu(111) substrate during measurements. Other porphyrinic systems, such as H₂TBPP on Cu(100) [35] present the formation of 2D islands in the middle of terraces at room temperature. In the NiTPP/Cu(111) system the molecular adsorption mechanism consists first of step edge decoration followed by the disordered 1D molecular chain starting to align with other NiTPP that adsorbs near chains. By losing mobility of the reported mobile phase of NiTPP, more molecules begin to interact to the chain and a 2D closed packed arrangement is formed. This behavior is enlightened in Figures 7A and 7B, for a coverage of approximately 0.2 ML, with the nucleated molecules being visible near the step edges.

Although molecules were not observed to nucleate in islands in the middle of the terrace, single molecules were observed in these regions (see Figure 7A). We attribute such behavior to two possibilities: 1) A foreign molecule. Since we have used a commercial molecule, they contain 1% of impurities. Some of these impurities might have been present at the time molecules were deposited. The strange electronic corrugation shown in Figure 7E, where it is not possible to image the lobes, corroborates to this fact. 2) It is a TPP molecule trapped in a terrace defect. Since the size of the molecule is bigger than the size of TPP, this explanation is ruled out.

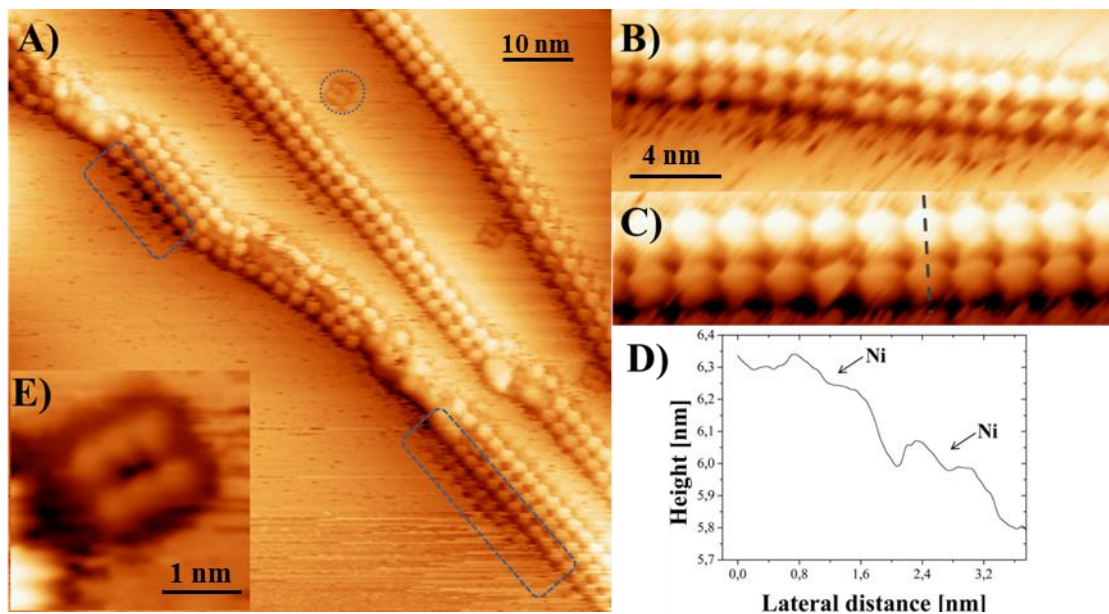


Figure 7: A) STM image ($85 \times 85 \text{ nm}^2$) of the transition between disordered 1D nanochains to 2D self-assembly with bias voltage of 1.5 V and tunneling current of 610 pA. The nucleated molecules in the lower terraces are inside the dashed rectangles. In dashed circle, an example of a foreign molecule. B) Zoom-in STM image ($22 \times 8 \text{ nm}^2$) of one of the lower terraces molecule adsorption with bias voltage of 1.5 V and tunneling current of 610 pA. C) Zoom-in STM image ($15 \times 4 \text{ nm}^2$) of the regular pattern of the double atomic height row, with bias voltage of 1.5 V and 340 pA. D) Line profile of the black line in C). It is observed that the molecule pattern is no longer disordered with the average distance between molecular centres (adjacent peaks) being $(1.35 \pm 0.03) \text{ nm}$. The depressions in the molecule sketch represent the nickel atom. E) STM image ($3 \times 3 \text{ nm}^2$, 0.8 V, 0.5 nA) of unusual molecular occupancy at the middle of the terrace, attributed to adsorption on a defect or being a different molecule.

When the terraces have diatomic height, it was observed that NiTPP still prefers to nucleate in the step edge and create a double molecular chain, as indicated in Figure 7 C. The metal atom of the TPP molecule is indicated in Figure 7 D in the line profile of the double nanochain as having a depression in its center. The Nickel center is measured as a depression due to the lower tunneling probability in the center, because of the electronic filling of the d_{z^2} orbital as concluded by Lu and Hipps [36]. Measuring the average distance between molecules on these observed nanochains shows that they possess an intermolecular distance of $(1.35 \pm 0.03) \text{ nm}$. This implies that whenever there is a higher density of molecules, their interaction starts to orient molecules, moving towards a regular assembly regime.

3.3.4 Two dimensional assembly and chirality

This study now focuses on higher coverage, when intermolecular interaction plays a key role on the self-assembly properties. Figure 8 A shows a typical large scale STM image for ~ 1 ML of NiTPP on Cu(111). The NiTPP assembles in an almost-square lattice, demonstrated by Figure 8 B, with unit cells of $a_1=(1.35\pm 0.04)$ nm by $a_2=(1.34\pm 0.04)$ nm and their relative angle being (85 ± 2) degrees. This 2D behavior is similar to the formation on the NiTPP/Au(111) [37], and CuTPP/Cu(111) [38]. Differently from Lieve et al [37], no parallelogram structure was found on this system, indicating that due to a higher reactivity with the substrate, molecular arrangements that require lower interaction between molecules and substrates are undermined.

In the representation of the NiTPP in Figure 8 A and B, the main intermolecular interaction was depicted as being caused by the so called T-type interaction, as concluded by Near edge x-ray absorption fluorescence spectroscopy and density functional theory studies performed by Auwerter et al [39] in the CoTPP/Ag(111). The T-type interaction, shown in Figure 8 D, occurs when the C-H group of the phenyl structure interacts strongly with the center of the π -system of the phenyl structure of an adjacent NiTPP. Another possible intermolecular interaction would be the π -type interaction (Figure 8 D), when the phenyl structure from different molecules are parallel to each other, thus creating an overlap in the final molecular orbital, but due to geometric reasons the π -type interaction cannot occur.

The explanation for an achiral molecule to form a chiral superstructure lies on the intermolecular interactions. As explained by Raval et al [40] the π - π interaction between the phenyl groups of different molecules produces a tilt of the molecule so that one of the axis of NiTPP, formed by opposed nitrogen atoms, is rotated by $\nu=(25\pm 2)^\circ$ with respect to one of its unit cell vectors. The hydrogen repulsion between phenyl and pyrroles leads to a change in the conformation of the macrocycle of the porphyrin.

The NiTPP molecule appears to adsorb in the saddle shape conformation on Cu(111), as evidenced in Figure 8 C. This can be concluded from the fact that the distance between opposite pyrroles is different than the distance between the other two opposite pyrroles, rotated 90° , as shown in the STM image. This difference is explained due to the fact that opposite pyrroles are twisted upwards, while 90° rotated pyrroles are twisted downwards. The possibility of the porphyrins being in the saddle or ruffled configuration has been treated on literature [41; 42].

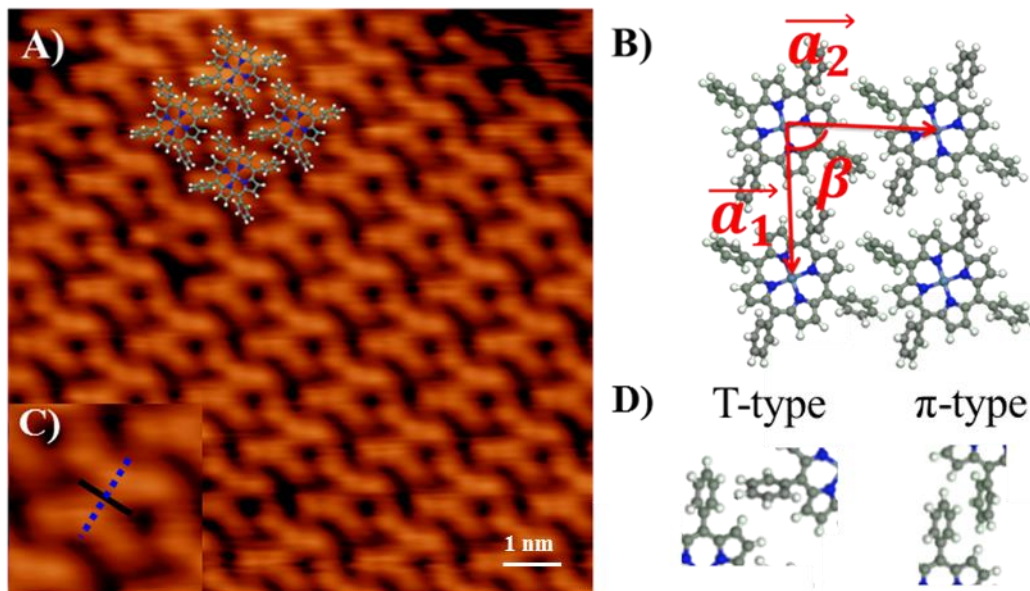


Figure 8: NiTPP on Cu(111) at monolayer coverage. A) STM image ($10 \times 10 \text{ nm}^2$) showing the 2D closed-packed self-assembly of NiTPP on Cu(111) with bias voltage of 1.2 V and tunneling current of 0.3 nA. It is possible to see the 4-fold symmetry of the NiTPP. B) Scheme of the unit cell with vectors $a_1 = (1.34 \pm 0,05) \text{ nm}$ and $a_2 = (1.35 \pm 0,05) \text{ nm}$ with their respective angle being $\beta = (85 \pm 1)^\circ$. C) NiTPP saddle-shape conformation shown in detail ($2 \times 2 \text{ nm}^2$). The distances between opposite pyrroles (dashed blue and full black lines) appear to be different. D) Representation of the T-type and π -type, when two phenyls of different molecules are either perpendicular or are parallel to each other, respectively.

In the monolayer coverage it was observed the existence of chiral domains in the superstructure formed by NiTPP. These domains will be denoted S and S'. Figure 9 A displayed a large area STM image with the chiral domains shown. They were found to be rotated by $\alpha = (10 \pm 2)^\circ$ from the $\langle -110 \rangle$ direction of the Cu(111) crystal. Figure 9 B shows a small area STM image of the NiTPP arrangements in the S and S' domains.

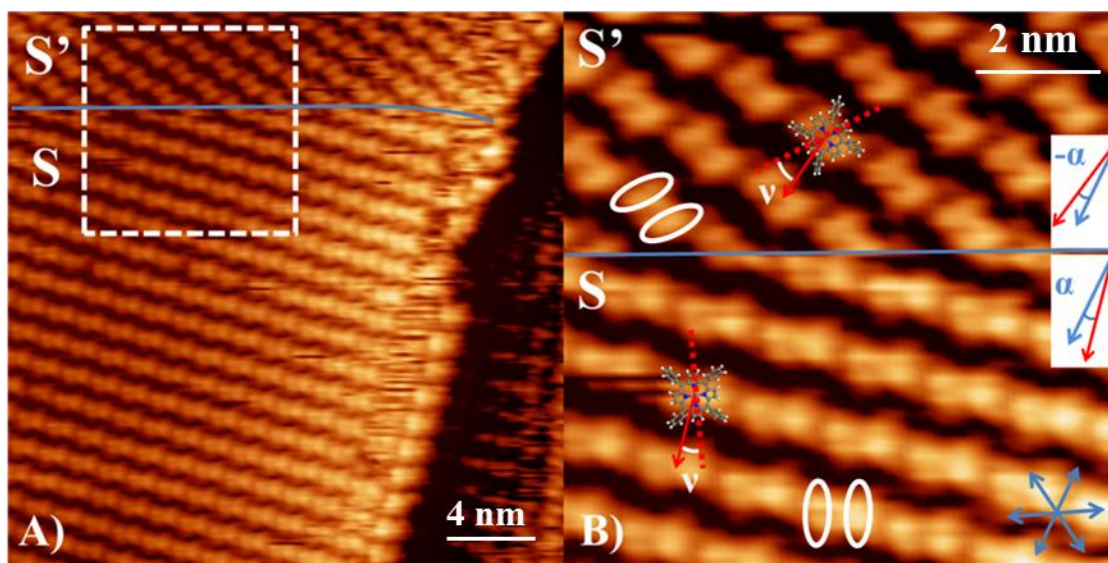


Figure 9: A) Large area STM image ($25 \times 25 \text{ nm}^2$) with bias voltage of 1.2 V and tunneling current of 120 pA showing the S and the S' domains in which NiTPP assembles. B) Small STM image ($9 \times 9 \text{ nm}^2$) of the dashed area in figure A. It is possible to resolve both existing domains and compare one of their vector lattice with the blue arrow, representing one of the $\langle -110 \rangle$ main directions in Cu(111). The angle formed is $\alpha = \pm(10 \pm 2)^\circ$, while the angle formed by one of the main axis of the NiTPP to the lattice vectors of the superstructure is $\nu = (25 \pm 2)^\circ$.

3.3.5 XPS analysis of NiTPP/Cu(111)

In order to study how the chemical environment of NiTPP is modified due to interaction with the copper substrate, different coverage were analyzed with XPS, ranging from close to monolayer depositions to the multilayer regime. The former gives information about the molecule-molecule and molecule-substrate interaction. The latter gives information mostly on molecule-molecule interaction. In the low submonolayer coverage, the signal from C 1s was weak because of low electron counts. The multilayer coverage was calculated as being 8 ML, by the attenuation of the Cu $2p_{3/2}$ signal, as observed in Figure 10.

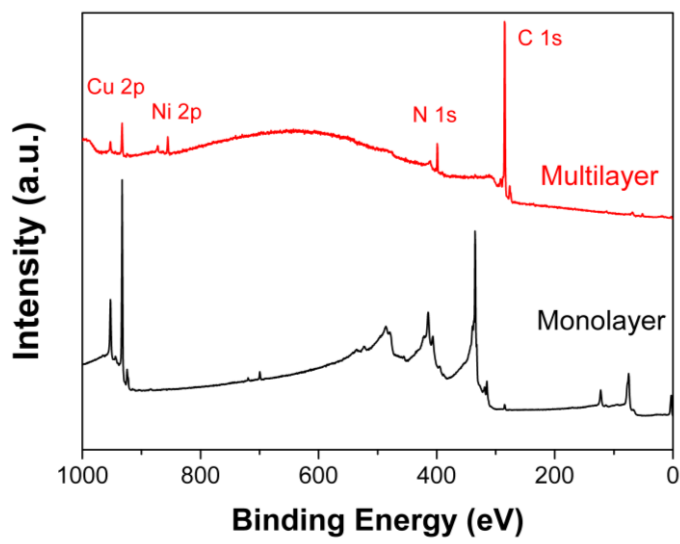


Figure 10: XPS Spectra for different NiTPP coverage. Approximately 1 ML of NiTPP is presented in black and 8 ML of NiTPP is presented in red. By the attenuation of the Cu $2p_{3/2}$ core line it was possible to estimate this coverage. The major peaks of NiTPP are pointed out in the multilayer spectra and to be better visualized in the graphic each point had its intensity divided by four.

Analyzing separately the elements of NiTPP, it is observed a chemical shift between the monolayer and the multilayer regime. The XPS spectra for the Ni $2p_{3/2}$ has peaks centered in energies of 852.9 eV and 855.5 eV, respectively in the monolayer and the multilayer coverage, which represents a shift of 2.6 eV (Figure 11 A). The C 1s signal shows a chemical shift lower than 0.2 eV in the multilayer regime (Figure 11 B), while the N 1s peak suffers a shift of 0.5 eV between the same layered systems (Figure 11 C), both towards higher binding energies. The explanation resides in the fact that nickel is the atom in the molecule that more strongly interacts with the substrate, followed by nitrogen and carbon.

The multilayer signal of Ni $2p_{3/2}$ and C 1s core lines are in good agreement with data reported in the literature [29;43]. A chemical shift of 2.3 eV for the Ni $2p_{3/2}$ core line is observed for the monolayer configuration on Cu(111) compared to NiTPP/Au(111) [33]. This fact can be ascribed to the differences in the strength of the metal-molecule interaction.

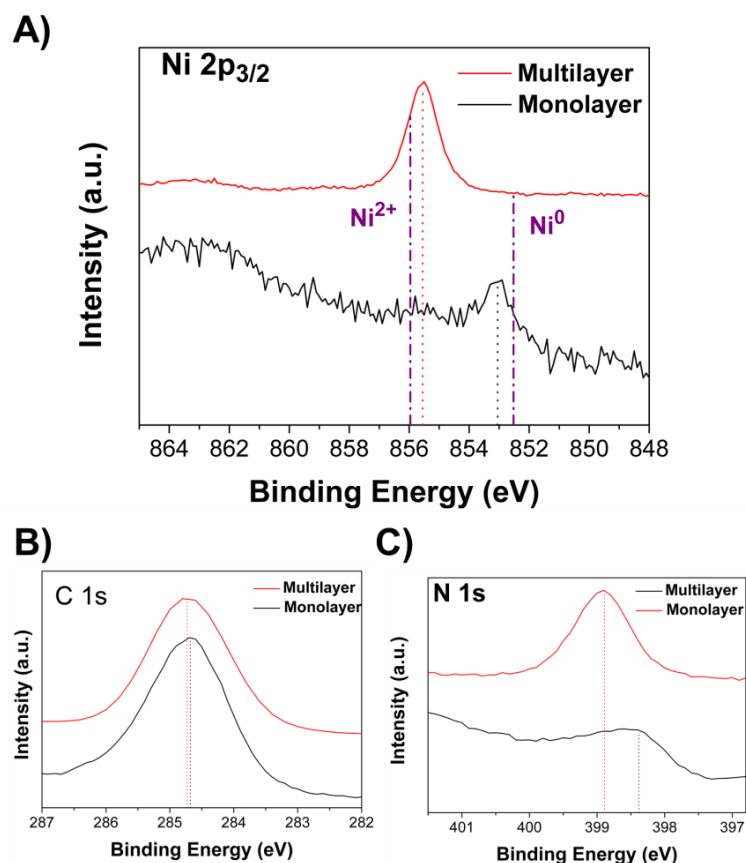


Figure 11: XPS spectrum for different chemical elements in NiTPP for monolayer and multilayer coverage. A) Spectra of Ni 2p, showing a chemical shift of 2.5 eV. In dash-point it is represented the peaks of both Ni⁰ and Ni²⁺ on Cu(111) [28]. B) Spectra of C 1s showing a chemical shift lower than 0.2 eV. C) Spectra of N 1s showing a chemical shift of 0.5 eV. Nickel is the atom that is more strongly bonded towards the Cu(111) surface.

It is possible to point out, through the observation of binding energies of different peaks, that when NiTPP is in the monolayer regime the peak position is similar to nickel in the null oxidation state, with binding energy of 852.5 eV on Cu(111) [44], acting as if it was in a metallic state. Upon higher coverage, the Ni 2p_{3/2} peak shifts as described above and behaves close to the nickel in the oxidation state of +2 state, with binding energy of 856 eV on Cu(111) [44], as indicated in Figure 11 A. This might be understood that each NiTPP molecule is bonded to the substrate as to acquire electrons, presenting itself as an important mechanism for the anchoring of the molecule on the substrate. The shift of Ni 2p in the XPS can instead be understood to be the result of a hybridization between the Ni 3d orbitals with the substrate orbitals similarly observed for CoTPP/Ag(111) [45]. The conclusion for the principal mechanism that results in chemical

shift of nickel observed in XPS requires more experiments. Simulations are being performed by Professor Roberto H. Miwa from the State University of Uberlandia (Brazil), and so far the results obtained present evidences for the hypothesis of hybridization of states.

3.4 NITPP ON VICINAL GOLD

Towards the envisaged idea of controlling the dimensionality of the self-assembled structures on a surface, it is possible to utilize several mechanisms, including the growth mediated via the step edges [46], and the use of electronic corrugation of the surface to guide the attachment of molecules [47]. It was shown in the previous section, regarding the step edge decoration of NiTPP/Cu(111), that it is possible to have the NiTPP wires oriented in the position at which the terraces are terminating. But in the case of oriented wires, the proper control of the orientation of such wires is crucial.

One possible route to engineer NiTPP orientation is the use of vicinal surfaces. Such surfaces possess atomically flat terraces separated by steps. Due to the presence of steps, the diffusion barrier along the step edge is enhanced due to the Ehrlich-Schwoebel barrier [48] and creates difficulties towards nanosystems crossing over the steps.

In this section we discuss about vicinal surfaces, in particular the chosen Au vicinal surfaces Au(332) and Au(788) and the adsorption behavior of NiTPP for different coverage.

3.4.1 Vicinal surfaces

Vicinal surfaces are low index surfaces which have undergone a miscut angle. If the cut is made in a respective angle at which close-packing atomic arrangement can occur, this yields flat terraces.

Due to minimization of the surface free energy, the surface can become a step bunch, which is the terminology for a faceted structure. Another possibility, and the possibility exploited here is that the surface presents regular arrays. In literature [49] the regular arrays are known to be formed and maintained because of the repulsion between steps, which avoids step-bunching.

Two of the main components for the step-step interaction are the elastic and electronic contributions. The electronic interaction exists because of the abrupt change in topography of the surface. This redistributes the charges and creates dipoles at the steps. Such effect is called the Smoluchowski effect [50]. As shown via angle resolved photoemission and STM measurements [51], there is an electronic confinement at the steps because of the electronic interaction between steps. The elastic interaction occurs due to the lower coordination number of atoms at the step edge. These atoms relax, in comparison to those in the terrace and this induces strain fields along the terrace. The strain field produces this step-step repulsive interaction.

In order to properly define a vicinal surface there are several quantities that lead to its correct assessment. Here, we are going to define the important parameters as being the terrace width L and the miscut angle δ , both shown in Figure 12 A. With such quantities one can obtain the orientation of the vicinal surface along the number of atomic rows each terrace possesses. We have employed Au vicinal substrates from Mateck (error in the miscut angle lower than 0.1°). The miscut angle of the crystals used in this work was performed along the $[-211]$ direction and the terraces run across the $[01-1]$ direction, as shown in Figure 12 B.

The crystals used in this work were Au(332) and Au(788), with miscut angle to the $[111]$ direction of 10.0° and 3.5° , respectively. The terraces should be composed of 5 and 15 gold atoms in a row, respectively.

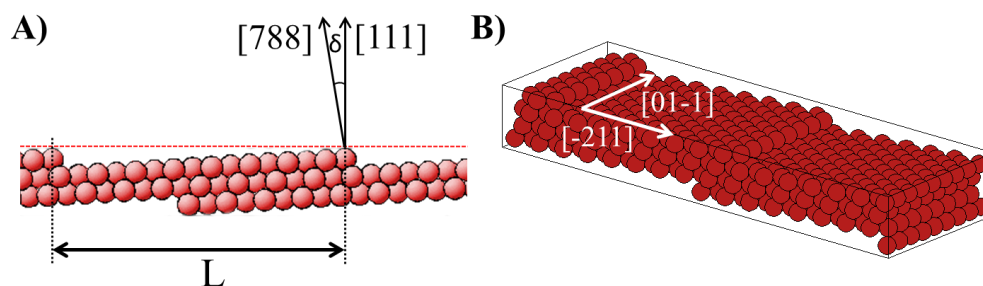


Figure 12: Schematics of a Vicinal Au surface using Au(788) as an example. A) Profile view of Au(788) showing a step, the miscut angle δ with respect to $[111]$ direction and the terrace width L . B) Perspective view of Au(788) with two steps being depicted. The orientation of the steps is in the $[-211]$ direction and the terraces grow on the $[01-1]$ direction.

Surfaces were cleaned and prepared with the standard procedure in UHV, starting with sputtering with argon ions and then annealing. But due to the fine limit between step-bunching and step repulsion, the amount of energy given to the surface has to be increased slowly – reaching 400 °C within 20 min of the start of the annealing process.

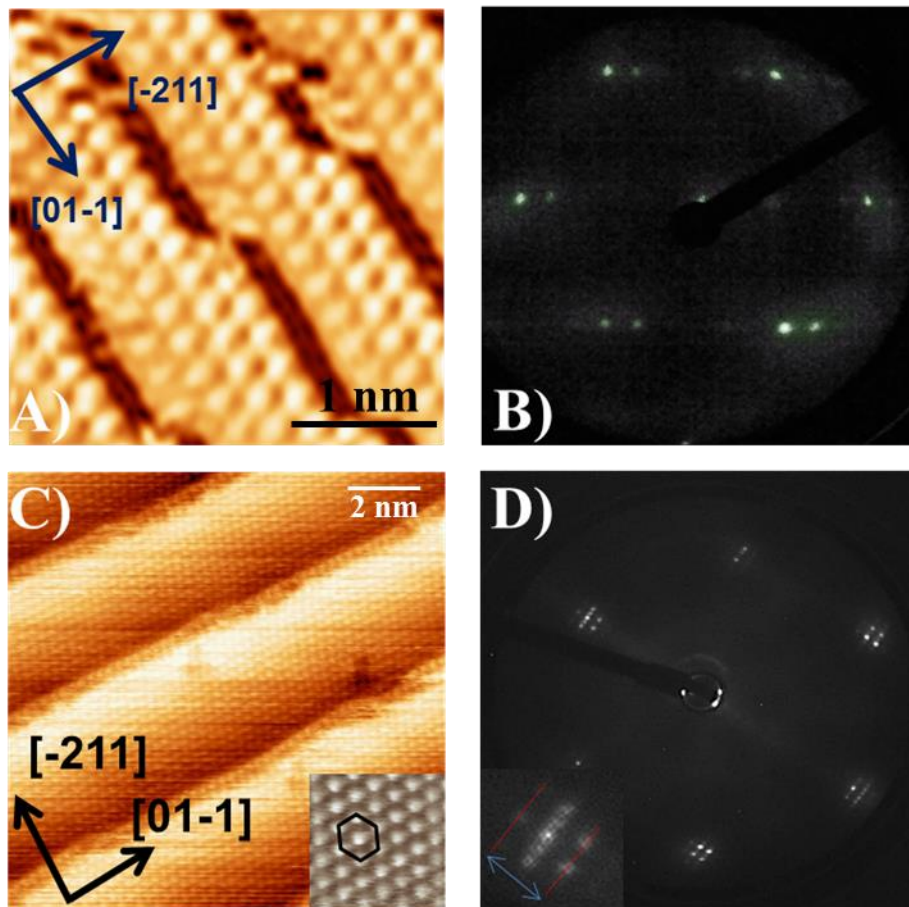


Figure 13: Experimental characterization of Au(332) and Au(788). A) STM image ($3 \times 3 \text{ nm}^2$, 1.7 V, 0.3 nA) of the atomic resolution of Au(332) [52]. The atomic distance between gold atoms was measured as being $(2.7 \pm 0.1) \text{ \AA}$ and the terrace width $L = (1.4 \pm 0.1) \text{ nm}$. B) Low energy electron diffraction of the cleaned substrate taken at 117 eV, showing the hexagonal symmetry of the fcc Au in the (111) direction. The inner structure of the points is attributed to the existence of steps. C) STM image ($12 \times 12 \text{ nm}^2$, 0.4 V, 1.7 nA) of the atomic resolution of Au(788), with an inset of $(1.8 \times 1.8 \text{ nm}^2)$. The Au-Au distance was measured as being $(2.8 \pm 0.1) \text{ \AA}$ and the terrace width $(37 \pm 2) \text{ \AA}$. D) Low energy electron diffraction of the cleaned substrate taken at 71 eV, showing the both the hexagonal symmetry of Au(111) and the inner structure along the red line is due to the periodicity of the terraces, the blue arrow also shown on the inset amounts to the periodicity of the steps.

Characterization of the cleaned vicinal substrates allows the proper assessment about their orientation, in which they were bought, and also on the quality of the *in situ* UHV preparation of the surface. To that extent, we have employed three surface sensitive techniques. XPS guaranteed the absence of contaminants on the surfaces within the experimental conditions (data not shown here). With low energy electron diffraction (LEED) we can obtain the crystallographic orientation of the surface. Besides observing the hexagonal packing of Au atoms, as shown in the LEED pattern of Figure 13 B and D, the diffraction pattern shows points splitting in two directions (along the red line on the inset of Figure 13 D). The reason for this splitting is because instead of the surface consisting of large low index planes, it consists of regular stepped surface. This enables qualitative measurements of the regularity of the terrace width and length.

The third (and most employed in this work) surface sensitive technique, STM, was used to characterize Au(332) and Au(788) more quantitatively. Along with obtaining atomic resolution images, displayed on Figure 13 A and C, a lattice constant of (2.7 ± 0.1) Å and (2.8 ± 0.2) Å was measured, respectively. These values are in good agreement with the ones reported in literature for the same vicinal surfaces [52]. The terrace width was calculated using several STM overviews and the widths obtained are (1.4 ± 0.1) nm for Au(332) and (3.7 ± 0.1) nm for Au(788). Both appear in accordance to the literature.

An interesting finding in the STM images is the presence of kinks only in Au(332). We argue that in this case, kink creation depends on the power given in the surface reconstruction during annealing. The equilibrium between merging terraces and step-step repulsion, along with strains in the surface, creates such kinks. By lowering the power given in the annealing process such kinks were reduced.

Au(111), due to non-uniform stress in the surface, is reconstructed in the so-called ‘herringbone’ reconstruction [53]. But since its periodicity is bigger than the Au(788) terrace widths, this cannot occur. Au(788) also possesses hcp and fcc sites as in the herringbone reconstruction [54]. The periodicity between hcp and fcc was measured to be approximately 71 Å [52] and typically yields preferential adsorption sites for single molecules. In Figure 13 C the last atomic row in the terrace of Au(788) is seen to be far away in comparison to the other atomic rows. This is a discommensuration line and it is caused by the same non-uniform compression mechanism. On Au(332) no reconstruction was observed, and the explanation is that the terraces are smaller.

3.4.2 Submonolayer adsorption of NiTPP on vicinal Au

In order to create parallel and equidistant wires we used the non-reactive vicinal gold substrate. By adsorbing in submonolayer coverage and measuring the surface with the STM it is possible to infer on the growth mechanism. For Au(332), the STM micrographs show that molecules prefer to nucleate in small islands, of averaged area 85 nm^2 for 0.3 ML coverage. At each vicinal terrace of Au(332) only one molecule can adsorb, since the width of the measured terrace is $(1.4 \pm 0.1) \text{ nm}$. As shown in the Figure 14 A and E the molecules are nucleating in a parallelogrammic lattice, with vectors equals to $a_1 = (1.47 \pm 0.04) \text{ nm}$ and $a_2 = (1.38 \pm 0.05) \text{ nm}$ and their relative angle being (75 ± 3) degrees.

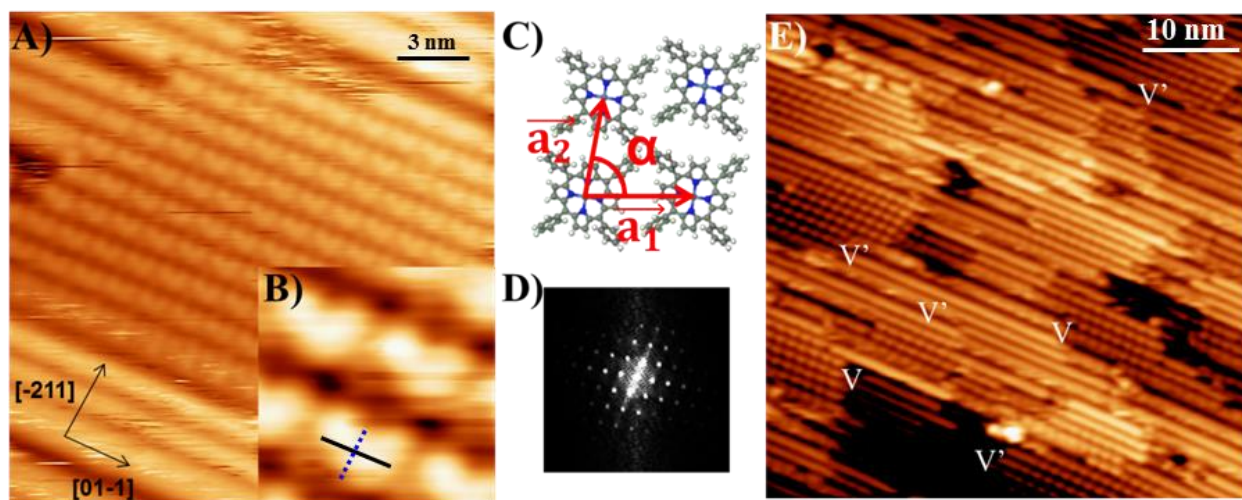


Figure 14: NiTPP on Au(332) at submonolayer coverage. A) STM image ($20 \times 20 \text{ nm}^2$, 1.9 V, 160 pA) showing molecules nucleated in small islands, of averaged size $(85 \pm 20) \text{ nm}^2$ coexisting with the clean Au vicinal surface. B) Zoom-in STM image ($3 \times 3 \text{ nm}^2$, 1.9 V, 160 pA) revealing the inner structure of NiTPP and the difference in electron density between perpendicular pyrroles (black and dashed blue lines), which is due to the saddle shape conformation. C) The parallelogrammic 2D lattice made of NiTPP has lattice vectors $a_1 = (1.47 \pm 0.04) \text{ nm}$ and $a_2 = (1.38 \pm 0.05) \text{ nm}$ and their relative angle is (75 ± 3) degrees. D) Fast Fourier transform as proof of the parallelogrammic lattice. E) STM overview ($50 \times 50 \text{ nm}^2$, 1.7 V, 100 pA) showing the V and V' chiral domains. The image was saturated so that the domains could be seen.

Due to phenyl-phenyl interactions, as was the case for NiTPP/Cu(111), there is an angle between the main axis of NiTPP with respect to the lattice vectors of the rhombic structure. This

provides the same chiral phenomena as in Cu(111). In Figure 14 E it is possible to visualize both types of parallelogrammic domains, here denoted V and V'.

In Figure 14 A there are streak features on the image. This is an evidence of the coexistence of a mobile phase along with the nucleated islands. Such a phase creates difficulties towards the scanning process, since it is easier to pick up a molecule with the tip or even to force the STM scanner to approach or retract the tip in a quick fashion as the feedback loop becomes idle for a few scanning points.

The difficulties in obtaining high-resolution quality images on this coverage yield poor information on respect of the molecular conformation. In the majority of STM scans the NiTPP molecule exhibits a conformation similar to the saddle shape, as pointed out in Figure 14 B, where the distance between perpendicular pyrroles is different.

For the Au(788), due to the width of the terrace being approximately three times bigger, one might suggest the existence of more terrace area for molecules to nucleate in comparison to Au(332). However, the increase in terrace width should also provide a higher mobility for nanosystems to diffuse along the terrace. And this fact was one of the major problems in scanning NiTPP on Au(788) for low coverage.

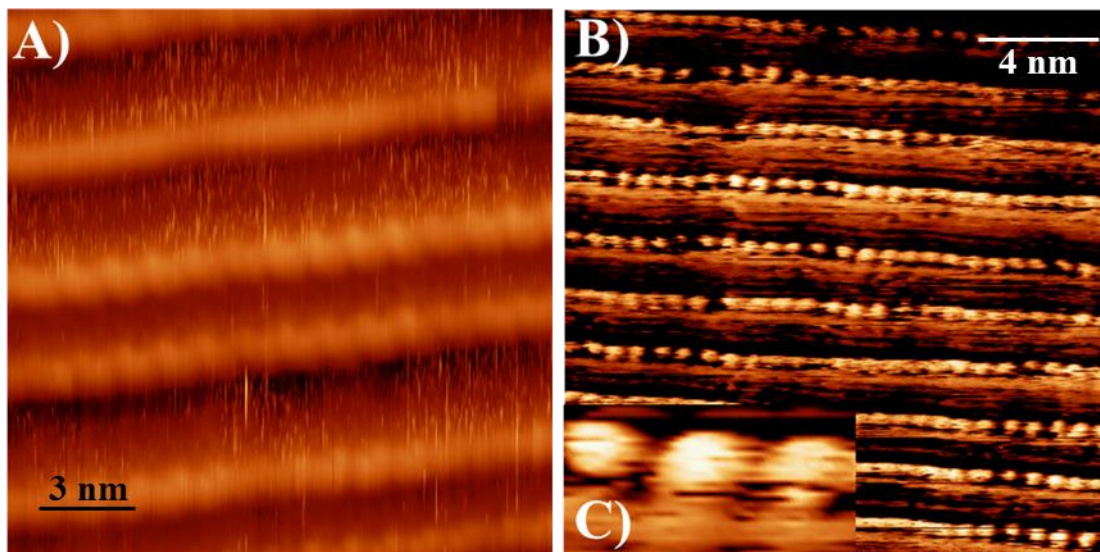


Figure 15: NiTPP on Au(788) at submonolayer coverage. A) STM image ($17 \times 17 \text{ nm}^2$, 1.3 V, 100 pA) showing molecules adsorbed at the step edge. B) STM image ($18 \times 18 \text{ nm}^2$, 1.1 V, 100 pA) with a different submonolayer coverage. Both images present different amounts of molecules which have not undergone adsorption along the terrace. This fact yields the streak features in the STM measurements. C) Zoom-in on three adsorbed NiTPP molecules ($4 \times 2 \text{ nm}^2$).

Figure 15 shows the topographic images for NiTPP/Au(788). It is possible to observe a high density of streak features on the image, which appear as noise in the topographic image. This can be attributed to the presence of a mobile phase, since now molecules can also diffuse along the terrace. At the step edges it is possible to observe rounded entities. We assign such features as being adsorbed NiTPP.

For such small coverage, no XPS spectra could have been observed due to the low signal from molecule's elements that reaches the XPS. So no information could be given that the rounded features presented here are in fact NiTPP. In order to preserve our results, prior these measurements, we deposited a higher coverage and calculated the ratio between carbon, nitrogen and nickel. The results are in accordance with the expected ratio of NiTPP.

In the scope of our main goal, it was possible to produce parallel equidistant nanowires of NiTPP. This was the major outcome that was envisaged in our initial project that was sent to FAPESP (grant number 2012/16860-6). Unfortunately, even at low coverage, it was difficult to obtain a coverage such that would only attain the specific amount of NiTPP that could adsorb on the step edges, without the occurrence of a mobile phase. On literature, no adsorption on the step edge of vicinal surfaces has been shown at room temperature. Cobalt-phtalocyanines and also a perylene derivative have been shown to self-assembly at the step edges of Au(788) [55]. However, both experiments were performed using low temperature scanning tunneling microscopy.

3.4.3 Mono and multilayer coverage on vicinal Au

For monolayer coverage of NiTPP on Au(332), the domains of nucleated NiTPP form the same parallelogrammic lattices V and V', as shown in Figure 16 A, with the same lattice constant values. We observe that the average size of domains is (230 ± 40) nm² which is higher than in the submonolayer case (~ 85 nm²). This suggests that the nucleation energy of a molecule that is not in an already nucleated island is lower than the energy required to create different molecular islands. Another observation from our STM images is that most of the times at which there is a terrace end, the orientation of the domain is unaltered. Such fact suggests that the interplay between all the interactions in the molecular self-assembly, molecule-molecule interaction is stronger in comparison to molecule-substrate interaction.

In the multilayer regime, NiTPP on Au(332) present two interesting features. Besides the parallellogrammic symmetry, due to the decoupling to the substrate, secondary and tertiary layered domains present also squared domains, named here as S-domains. This domain is represented in the STM image overview in Figure 16 B. The size of the lattice vector was measured to be equal to (1.37 ± 0.09) nm and it is comparable to the ones obtained for NiTPP on Au(111) [37]. In the few STM images with high resolution, it is possible to observe the two-lobe symmetry of the adsorbed molecules. This is an evidence of the saddle shape conformation, as seen in Figure 16 C, and indicates that for higher coverage the conformation of NiTPP is kept unchanged.

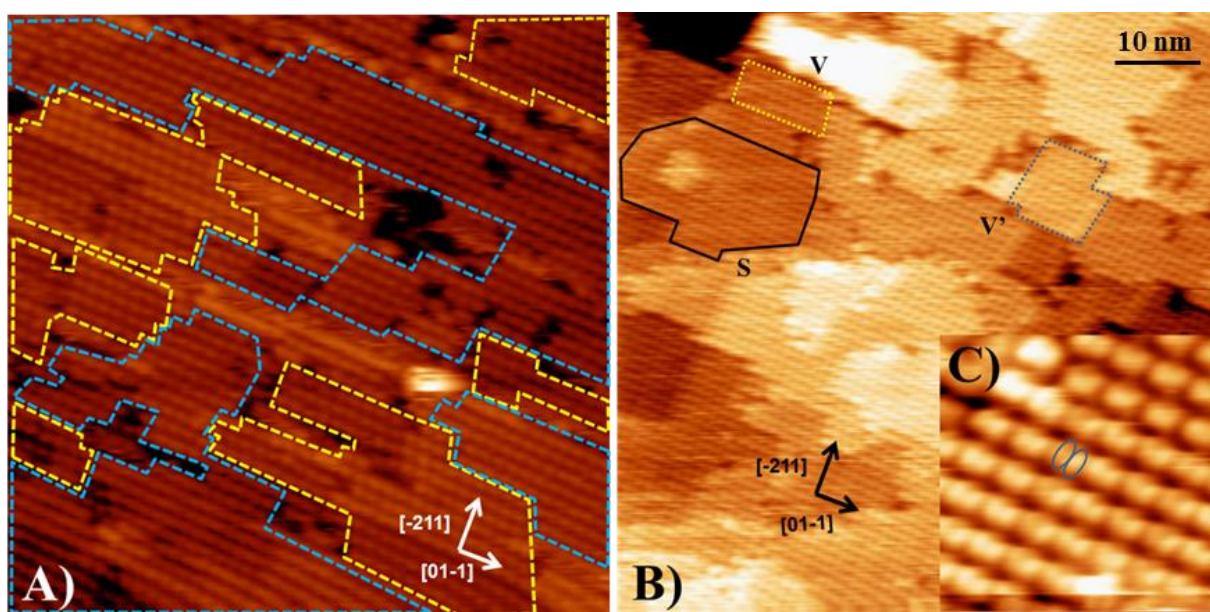


Figure 16: NiTPP on Au(332) at mono and multilayer coverage. A) STM image (50×50 nm², 1.3 V, 100 pA) of monolayer coverage of NiTPP. The molecules are arranged in the same parallellogrammic domains V (dashed blue) and V' (dashed yellow) as in the submonolayer coverage. The average domain area is (230 ± 40) nm². B) STM image (70×70 nm², 1.7V, 70 pA) of multilayer coverage of NiTPP. Besides orienting in V and V' domains, the decoupling to the substrate creates a square domain, called S. C) Zoom-in STM image (11×11 nm², 1.2 V, 100 pA) of NiTPP in the multilayer coverage showing the two lobe symmetry. This is a fingerprint of the saddle shape conformation of the molecule.

XPS results comparing the binding energy of core levels of C 1s, N 1s and Ni $2p_{3/2}$ in the monolayer and multilayer coverage of NiTPP remain unchanged (except for the attenuation of the Au 4f signal). The physical meaning of this information is that the interaction and eventual hybridization of orbitals of NiTPP due to being absorbed on Au(332) is nonexistent.

For NiTPP on Au(788), the measured terrace width was (3.7 ± 0.1) nm and the size of the molecule of 1.2 nm means that up to three molecules can assemble on each vicinal terrace. STM reveal that each terrace is composed of three molecular rows. Only two of these rows could be fully assigned. They form a square lattice, similar as in the case of NiTPP/Cu(111), shown in Figure 8. Their average lattice parameter is (1.41 ± 0.07) nm and their relative angle was measured as being equal to $(86\pm 4)^\circ$ (Figure 17 C). Molecules orient their main axis with a relative angle of $(15\pm 2)^\circ$ to the orientation $[-211]$ as depicted in Figure 17 E. And this yields chiral structures, shown in Figure 17 F. We assign such lattice formation due to competition between T (attractive) and π - π (repulsive) interactions between different phenyls of the molecules.

The proper assignment of the configuration of the third row is trickier in the sense that its area is lower, (0.98 ± 0.09) nm², than the expected value of the molecule in a plane, 1.44 nm². This is a clear evidence that molecules are rotated due to the step edge occurrence. By obtaining the ratio of this areas it is possible to estimate the angle between the terrace and the molecule main axis as being equal to $(47\pm 3)^\circ$, as shown in Figure 17 D. The orientation of the molecules at the step edge via STM is also trickier since we obtain a view from perspective. In this sense observing the top side of the molecules, which lies in the plane defined by the upper terrace, it possesses three protrusions (blue line in Figure 17 B). We assign the outer protrusions as being phenyl rings and the center one to the pyrrole. In the bottom region of adsorption of the molecule only two protrusions can be visualized, both are attributed to two phenyl rings. All phenyl rings are depicted as being blue crosses in Figure 17 B. The pyrrole in the bottom cannot be seen in such a configuration, because of its downward orientation. Throughout our measurements, the straight distance between the second row molecules of the square lattice and the molecules in the third row, which are rotated, were measured as being (1.21 ± 0.03) nm. The distance of the three molecular rows was measured as (3.88 ± 0.09) nm.

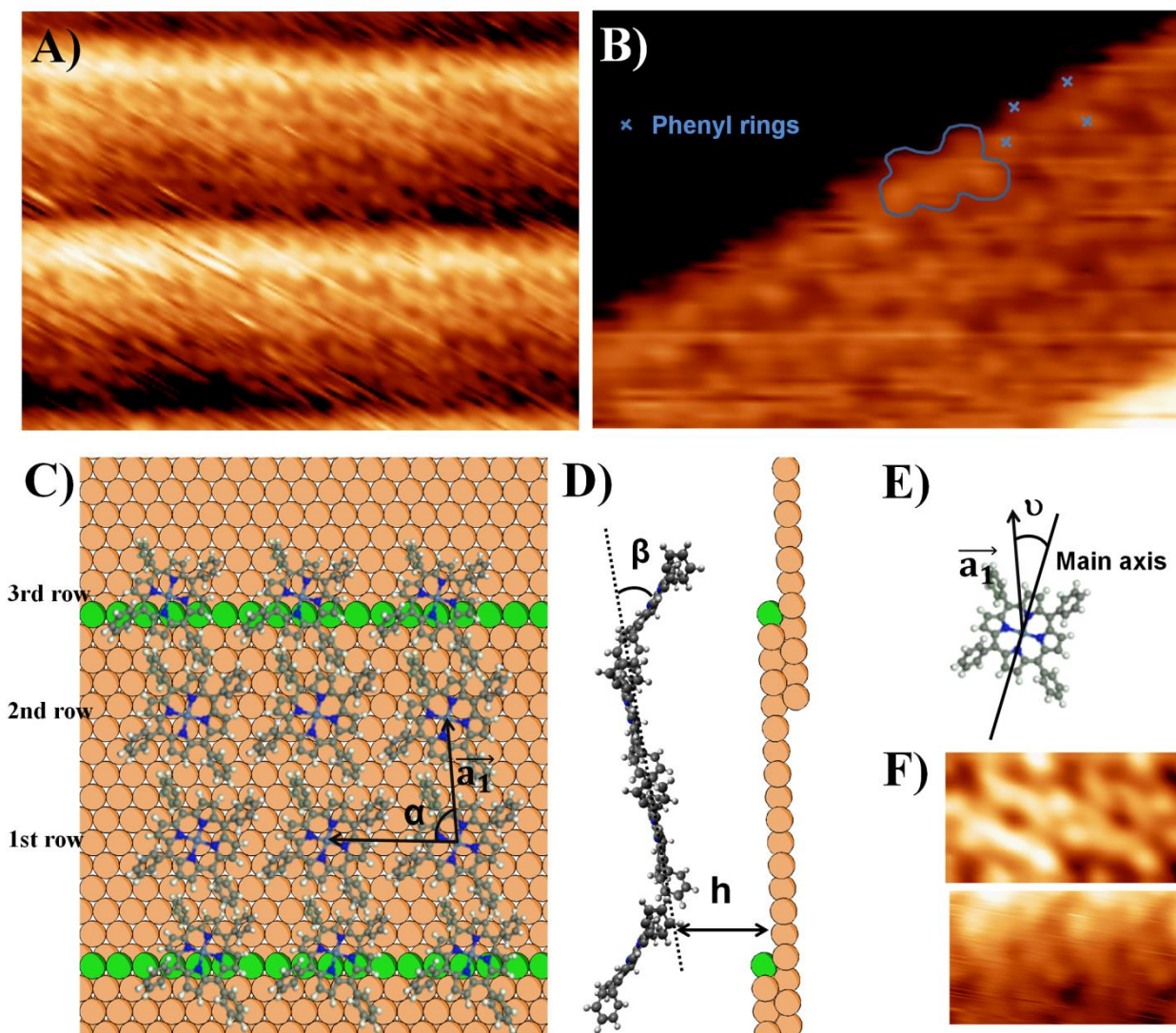


Figure 17: NiTPP on Au(788) at monolayer coverage. A) STM image ($12 \times 9 \text{ nm}^2$, 1.0 V, 600 pA) showing three molecular rows at every terrace. The first two form a square lattice and the third is at the step edge. B) STM image ($7 \times 5 \text{ nm}^2$, 1.1 V, 700 pA) highlighting one terrace. The blue line constitutes the NiTPP profile at the step edge and every phenyl is assigned with a blue cross. C) Top view model for NiTPP adsorption on Au(788). The first and second row forms a square lattice with both molecules in a more planar conformation. The third row adsorbs at the step edge. D) Side view model for NiTPP adsorption on Au(788), with the third row molecules rotated by $\beta = (47 \pm 1)^\circ$. The h distance between the molecules and substrate is unknown, further collaborations using computational models will be used to estimate the molecule-substrate distance. E) The first two molecular rows have their main axis rotated by $\nu = (15 \pm 2)^\circ$, this yields chiral structures. F) STM images ($3 \times 2 \text{ nm}^2$, 1.0 V, 700 pA) of chiral molecules along the Au(788) terrace.

Another observation which is possible to do with the STM measurements is the conformation of NiTPP. As shown in Figure 17 A, B and F the distance between pyrroles is the same.

This states that NiTPP is in the planar shape conformation. Such conformation suggests a higher energy state in comparison to the saddle shape conformation, because the organic part of the molecule can fix more strongly to the substrate via π -bonding. Similar systems were exemplified in literature, where by applying a voltage pulse it was possible to change from saddle to planar shape conformation [56].

Experimentally we found no difference between the mono- and multilayer XPS spectra. So this suggests that the bonding between macrocycles has similar behavior as the bonding between macrocycle-terrace and such conclusion cannot be explained, because the characteristics of the bonds should be different. Therefore, more experiments are needed to elucidate such behavior. Due to experimental difficulties the multilayer case of NiTPP/Au(788) was not obtained. The main reason is that in the obtained coverage, no tunneling condition was satisfied.

3.5 CONCLUSION OF NiTPP ON DIFFERENT METALLIC SUBSTRATES

In this work we have used NiTPP on different metallic substrates, from low index copper to vicinal Au. It was possible to obtain 1D adsorption of NiTPP on the step edges of Cu(111). Utilizing this prior knowledge, we could chose a surface that possessed enough electronic confinement as to guide molecules to adsorb at such places, as shown with the submonolayer coverage on Au(788). This opens up the possibility of testing magnetism properties in molecular wires as in the case of atomic wires grown in vicinal substrates [46].

The structural properties of 2D assemblies were also investigated. Due to the molecule being squared, most of the self-assembled lattices were also squares, as it was the case of NiTPP on Cu(111) and Au(788). On Au(332) the molecules, up to the monolayer coverage, nucleate in parallelogrammic lattices. It is interesting to note that when multilayer coverage is reached, NiTPP on Au(332) also presents squared lattice formations. This is a result of the decoupling of the substrate to the molecular layers.

Regarding molecular conformation, NiTPP on Cu(111) and Au(332) present a pronounced saddle shape conformation, which is a configuration that enables weaker bonds between the macrocycle of NiTPP to the substrate. On Au(788), a more planar conformation is obtained. This suggests a crossover between size of the terrace and molecular conformation and also opens up

the possibility to investigate the conformational behavior depending on the molecule distance to the step edge. Another possibility is the study of the structural and spectroscopic changes due to gas adsorption on NiTPP/Au vicinal surfaces.

4 BIMOLECULAR MIXTURE OF PHTHALOCYANINES

This chapter presents a part of the results obtained during the six-month student internship at the University of Basel, in Basel, Switzerland. The work deals with bimolecular mixture of commercial phthalocyanines (Pc) on different metallic substrates. All results were obtained using a Low Temperature Scanning Tunneling Microscope (Omicron Nanotechnology, GmbH) with a Nanonis control system (Specs GmbH) operated at 5 K.

4.1 INTRODUCTION

The approach of bottom-up architecting has recently received increasing attention and has motivated intensive investigations aiming at the controlled assembly of supra-molecular architectures at surfaces [27]. Various mechanisms to control molecular aggregation patterns are known. In general, assemblies at the solid/vacuum interface can be categorized by the type of intermolecular interactions involved in their formation: H-bonding, metal-coordination or covalent bonding [57]. For instance, by maximization of H-bonds as reported by Hipps [58], a co-assembled bimolecular system, composed of fluorinated phthalocyanines and regular phthalocyanines has been created on an oxygen-reconstructed Co surface [10]. This system, equipped with two different magnetic center metal atoms, has been demonstrated to act as a molecular spin-array, on which the magnetic information can be recorded by applying a chemical stimulus in the form of a gas dosed onto the sample.

The research presented here is focused at the co-assembly of Pcs on different and less reactive substrates. Such substrates help in creating alternative routes towards the control of highly ordered multi-component structures. Also, the oxygen termination needed to allow for molecular self-assembly on reactive molecular substrates as they have been used in the former study might modify the magnetic state of the ad-phthalocyanines. Thereby an oxygen free approach to manufacture 2D checkerboards provides a favorable alternative.

In this chapter, we present a new supramolecular system consisting of copper and manganese-phthalocyanines (CuPc and MnPc) assembled on a Bi reconstructed 2D film at Cu(100) sur-

face. The unique property of this system is the creation of a specific charge transfer dipoles which lead to self-sorting of bi-molecular mixture into a chess-board array.

4.2 PHTHALOCYANINES

The metallorganic molecules utilized in our study are metal-Pcs. These molecules were discovered in 1907 [59] and are similar to porphyrins in the sense that they also possess a planar macrocycle and a central metallic ion bonds to the inner nitrogen atoms. Each isoindole group is connected by a nitrogen atom, forming the macrocycle of the molecule, as depicted in Figure 18.

Pcs have been the first molecules measured with STM [60] due to their thermal and chemical stability. These molecules have important applications in the field of gas sensors [61]. The outer dimension of the diagonal across the Pc molecule measures 1.5 nm. The orbitals of the organic macrocycle hybridize with the central metallic ions. This hybridization splits the 3d orbitals of the transition metals commonly used at the center of Pcs.

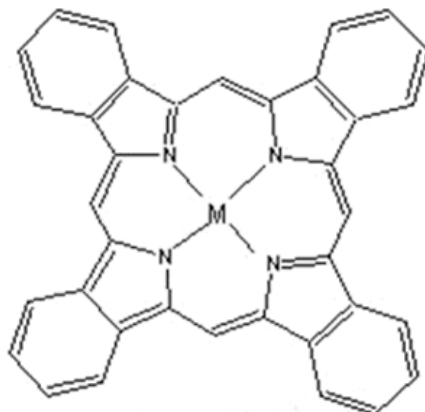


Figure 18: Phthalocyanine scheme. The molecule is composed of pyrroles connected to benzene rings. On the inside the molecule possess a cavity that can be functionalized with different metallic centers M.

4.3 TENTATIVE MOLECULAR SORTING ON SILVER (111) AND COPPER (100)

In our first trial, we have chosen Ag(111) as a substrate for its non-covalent interaction with adsorbed Pcs molecules, which causes their high diffusivity at room temperature. CuPc and MnPc have been chosen as the molecular building-blocks for constructing bi-molecular arrays due to their different d_z^2 orbital hybridization of the metal centers to the surface. This difference also allows for their identification in STM micrographs of mixed assemblies. It is known that the center of MnPc appears as a protusion, while the center of CuPc appears as a depression, at an energy of about 1 eV in STM micrographs[62]. Another important reason for using two distinct molecules is their different affinity towards forming a coordination bond with small molecules, such as CO or NO [28].

Deposition of a sub-monolayer coverage of both, MnPc and CuPc on Ag(111) results in single molecules randomly distributed over the surface as revealed by STM images taken at 5 K (Figure 19 A). This can be explained by the intermolecular repulsion, due to repulsive long range adsorbate-adsorbate interactions and the presence of the Shockley surface state on Ag(111). At higher coverage, close to 1 monolayer (ML), molecules are trapped in a molecular array. As it is shown in Figure 19 B, the molecules follow a random pattern and do not co-assemble in a chess-board pattern. The same behavior was observed on Cu(100), at submonolayer (Figure 19 C) and monolayer coverage.

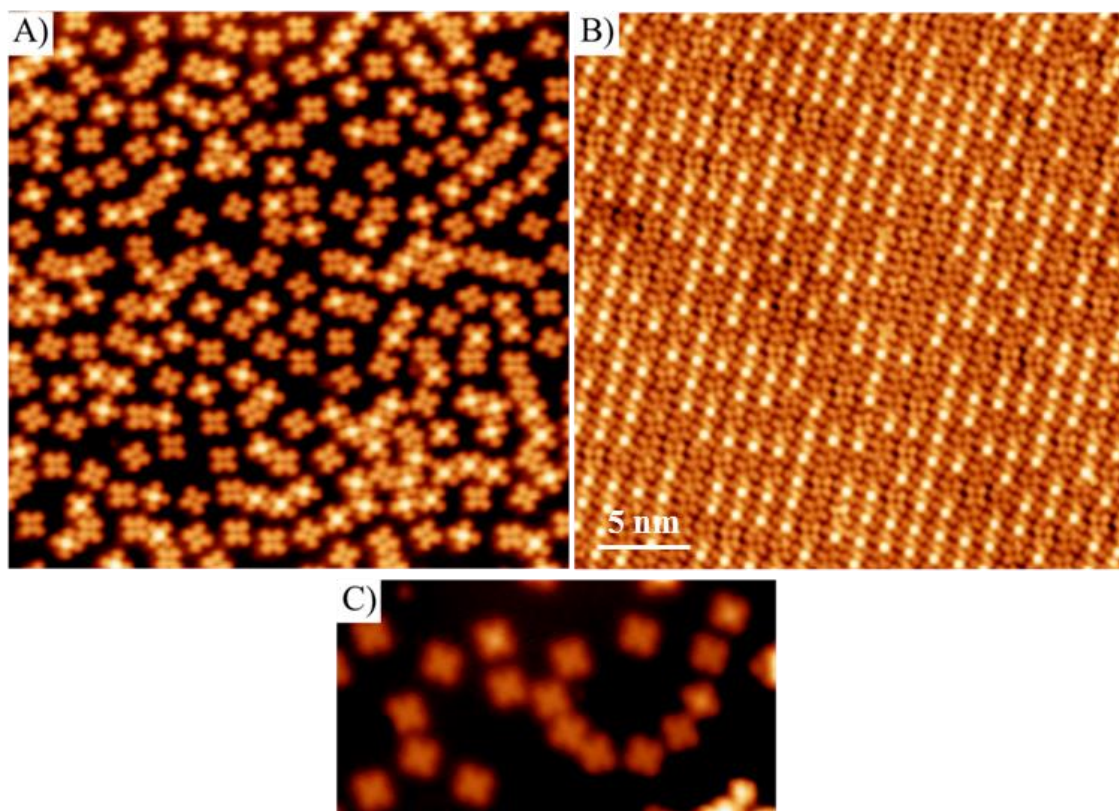


Figure 19: Bi-molecular mixture of MnPc and CuPc at different coverages on either Ag(111) or Cu(100) do not show any selective adsorption or sorting mechanism. A) At sub-monolayer coverage molecules are repelling each other on Ag(111) (STM: 30x30nm²; 1V, 10 pA). B) At full monolayer coverage of the bi-molecular mixture on Ag(111) the random sorting of the assembly is well identified (STM: 30x30nm²; 1V, 10 pA). C) Sub-monolayer mixtures on Cu(100) are likewise not assembled due to a repulsive inter-molecular interaction (STM: 10x20 nm², 1V, 10 pA).

4.4 ANALYSIS OF SURFACE OF BISMUTH ON TOP OF COPPER (100)

Instead of working with pure crystal surfaces, we decided to vary the electronic configuration along the surface. This can be obtained by providing different anchoring regions for different Pcs. In that sense we chose Bi/Cu(100) as substrate. Deposition of a submonolayer amount of Bi onto Cu(100) and subsequent annealing to ~200°C leads to the formation of a Bismuth-reconstructed surface. Several studies on this system attributed the observed p(10x10) superstructure to the periodic strain and relaxation patterns induced in the copper by the Bi top layers at different coverage [63, 64]. This reconstruction is composed by a grid of 10x10 Bi atoms which

are displaced concentrically on top of the Cu(100) atoms, therefore receiving the name p(10x10). At Bi coverage close to a monolayer, the Bi layer contains perpendicular dislocation arrays oriented in the [001] and [010] directions. The unit cell is a rectangular porous superlattice. Each unit cell contains four pores with dimensions of 1.6x1.8 nm². This choice of patterned substrate appears suitable to host Pc molecules due to their similar external dimensions i.e. ~1.5 nm². As shown in Figure 20 A, the STM image of Bi/Cu(100) shows three main features that correspond to a single pore. These features have different electronic intensities, as revealed by the STM image: pore, wall and cross (marked as regions A, B and C in Figure 20 A). In order to assess the electronic properties of this specific on-surface architecture, we have probed the local density of states (LDOS) by scanning tunneling spectroscopy (STS) and the relative work-function values on each region by I(z) spectroscopy.

The bismuth reconstruction exhibits a reduced work function (4.33 eV as measured via ultra-violet photoelectric spectroscopy (UPS) [65]), in comparison to the work function on bare Cu(100) (4.57 eV). The existence of different electronic corrugations along the bismuth surface causes corresponding changes in the charge redistribution at the Bi/Cu(100) interface. Physically, it means that the work function varies across the sample. By locally performing I(z) spectroscopy we have obtained the local work function values for different regions: (4.60±0.02) eV for the pore, (4.67±0.02) eV for the wall and (4.68±0.02) eV for the cross regions, shown in Figure 20 C. These values are higher than those measured by UPS (4.33 eV) earlier. Note however, that the STM work function measurement is modified by the tip-sample interaction in the tunneling junction. In our case, the work function associated with the Pt-Ir tips used in the STM ranges from 4.8 to 5.4 eV [66]. The following estimate now motivates our different results from the UPS results in literature: If we use an average value of the work function of tip as being 5.0 eV and consider the work function of the surface of Bi/Cu(100) as being the reported value in literature, 4.33 eV, this would provide a work function of 4.67 eV, when measured with the STM. This value of 4.67 eV is close to the values we have measured with I(z) spectroscopy.

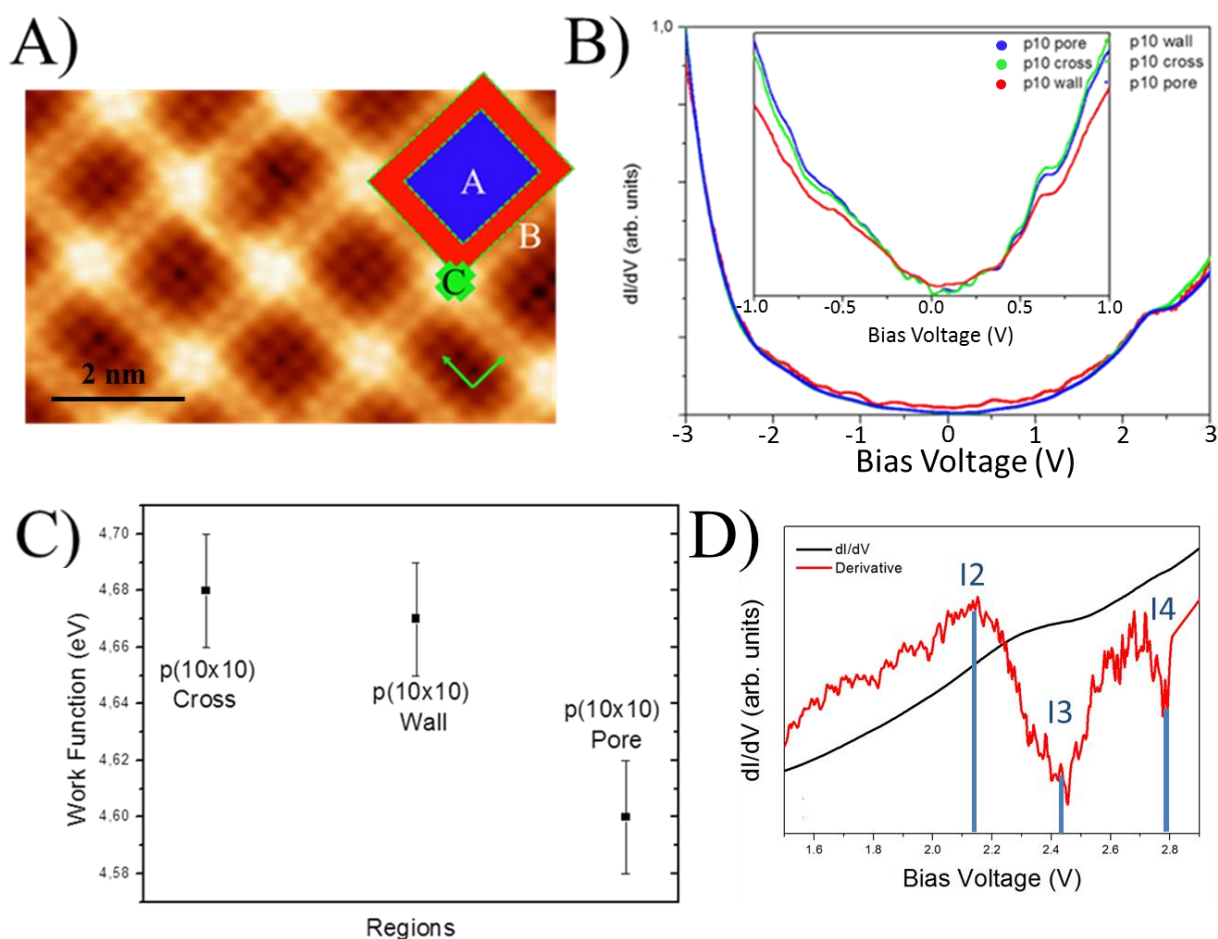


Figure 20: Structural and electronic properties of the Bi/Cu(100) surface. A) STM image of the monolayer reconstruction of Bi/Cu(100) ($8 \times 5 \text{ nm}^2$, 5 mV, 400 pA) indicating three different regions (A – pore, B – wall, C – cross). B) dI/dV measurements on different regions of the reconstruction: Blue, red and green curves were measured in the pore, wall and cross regions, respectively. C) Work function measurements for three different regions of the bismuth reconstruction. D) Example of STS spectrum with the respective numerical derivative. It is possible to highlight the three states of Bi. The maxima without further addressing is related to a copper state.

Alongside the characterization of work functions of Bi/Cu(100), we decided to analyze the surface states of bismuth at every region (pore, wall and cross), by recording dI/dV spectra and comparing the results to earlier reports in the literature [64]. Spectra shown in this thesis are the average of approximately 30 spectra each. As can be seen in Figure 20 B there are no major differences between the dI/dV curves, so in order to obtain the correct bismuth states we have performed numerical derivatives of the dI/dV spectra (Figure 20 D).

There is good agreement between our results and those obtained by high-resolution angle-resolved UPS performed on Bi as reported in the literature (Table 1). Technically, to find such

states we produced the numerical derivative of the STS (black line in Figure 20 D) and this yielded maxima and minima in localized bias voltages (example of peaks shown in Figure 20 D). Some of the peaks found in Figure 20 D are related to copper states. To perform trustable STS experiments it is necessary to obtain valid reference spectrum and such an agreement to the values reported in literature supports that our dI/dV maps can be used to perform background subtractions of the dI/dV maps of the molecules, heading towards a better understanding of molecular features.

Table 1: The Bismuth induced states on the p(10x10) reconstruction extracted from the dI/dV spectra and their comparison to literature values obtained with the use of HR-ARUPS measurements.

State name	Bi/Cu(100) Averaged [eV] from literature [64].	Bi/Cu(100) cross [eV]	Bi/Cu(100) wall [eV]	Bi/Cu(100) pore [eV]
I2	2.93	(2.81±0.02)	(2.87±0.02)	(2.81±0.02)
I3	2.62	(2.53±0.02)	(2.65±0.02)	(2.65±0.02)
I4	2.13	(2.15±0.02)	(2.14±0.02)	(2.15±0.02)

4.5 COMPARISON BETWEEN SINGLE MOLECULE ISLANDS AND BIMOLECULAR MIXTURES

A limited number of studies reporting on molecules at electronically nano-patterned substrates are available. Most of these studies involve graphene and boron nitride surfaces [67, 68, 69]. No self-assembled molecular system occurring on a bismuth substrate has been reported so far. After a thorough characterization of the atomically clean bismuth/Cu(100) surface and the formed reconstruction patterns, we decided to study the self-assembly of pure MnPc and CuPc on Bi/Cu(100).

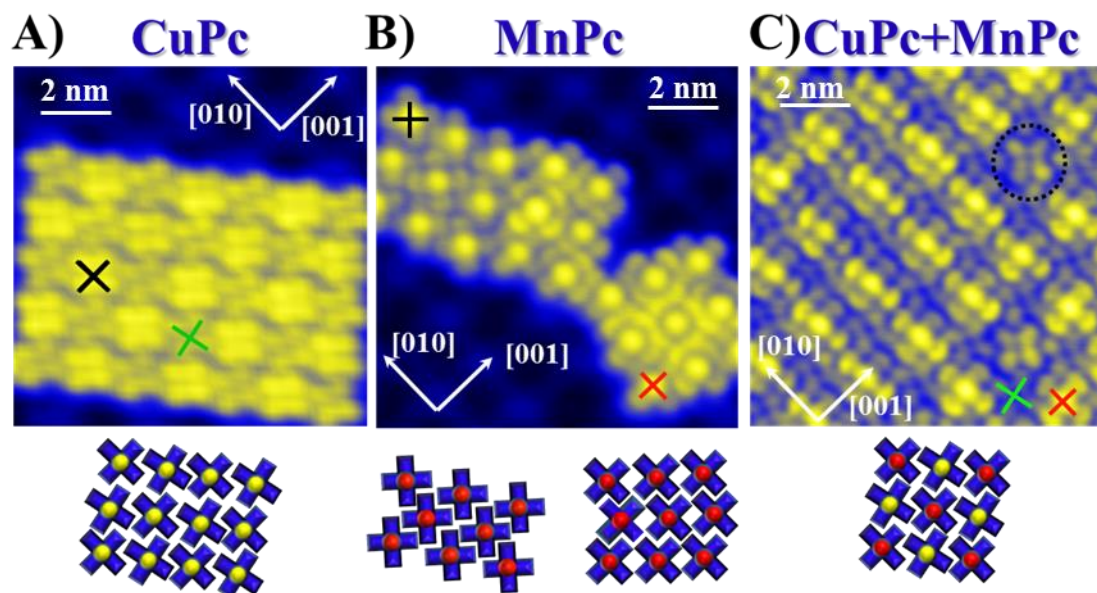


Figure 21: Self-assembly of single CuPc, MnPc islands and the bimolecular mixture of CuPc and MnPc. A) STM image ($10 \times 10 \text{ nm}^2$, 1 V, 10 pA) of the self-assembled CuPc island. There are two orientations of CuPc along the self-assembled islands, bright and dark. Depending on the orientation of CuPc, along the island, there is a contrast change in the STM image. Bright CuPc, highlighted with a black cross, have lobes oriented along the (010) and (001) directions. Dark CuPc, highlighted with a green cross, is rotated with respect to the Bright CuPc in 8° . B) STM image ($10 \times 10 \text{ nm}^2$, 1 V, 10 pA) of the self-assembled MnPc islands. There are two types of islands, each with different contrasts. The bright MnPc islands, highlighted with a red cross, exhibits lobes oriented along the main directions of the substrate. Dark MnPc islands, highlighted with a black cross, exhibits lobes oriented 45° rotated in respect to the main directions of the surface. C) STM image ($10 \times 10 \text{ nm}^2$, 1 V, 10 pA) of MnPc and CuPc co-assembled in a 1:1 ratio. Comparing the orientation of the molecules in the array, we observe that CuPc is oriented in the same way as dark CuPc in single islands, and MnPc has the same orientation as bright MnPc in single islands. The black dotted circle corresponds to a defect in our assembly, where a CuPc molecule occupies the position of a MnPc in the co-assembly.

The deposition of a submonolayer coverage of CuPc on Bi/Cu(100) resulted in the formation of small self-assembled islands, as depicted in Figure 21 A. Notably, the molecules appear with different brightness in the STM images (bright CuPc is indicated by the black cross and the dark CuPc with the green cross), depending on their orientation and position along the self-assembled island. The bright and the dark appearing molecules are rotated by $(8 \pm 2)^\circ$ with respect to each other. The bright CuPc takes an orientation of the lobes along the [001] and [010] directions as indicated by white arrows in Figure 21 A. The self-assembly behavior of CuPc on top of the Bi/Cu(100) reconstruction is completely different than directly on Cu(100) (Fig. 19 C), which

hints on the modified interaction of the molecules with the bismuth surface. The different contrast of CuPc also evidences different density of states or charge states located at the two molecules. A possible model is provided by periodic doping, since transition metal phthalocyanines had been shown to exhibit selective doping [70].

We also investigated self-assembled islands of pure MnPc. The self-assembly results contrast the behavior of CuPc. The islands of MnPc are smaller, typically consisting of nine molecules arranged in 3x3 islands. Bigger islands are constructed from the 3x3 islands that are not completely connected, but are rather aggregated via one or two linking molecules (as shown in Figure 21 B). We note that there are two types of islands which are e.g. recognized by their different orientation on the substrate (Figure 21 B). One type of MnPc islands, which is composed by bright molecules (highlighted with a red cross in Figure 21 B), exhibit an arrangement of the lobes along the [010] and the [001] direction. The dark type of MnPc islands, highlighted with a black cross, exhibits its lobes with an angle of $(45\pm 3)^\circ$ with the main direction of the Bi/Cu(100) film. Throughout our measurements, these two types of islands were always separated from each other. Careful assertion on the MnPc contrasts leads to an important observation: MnPc molecules that are co-aligned with the bismuth reconstruction exhibit not only different brightness but also a different molecular shape. It is not possible to discern contrast associable with the inner part of the MnPc molecule in the islands due to hybridization of the ligands at the energy which was used for the presented high-contrast STM micrographs.

Now we address the behavior of two phthalocyanines, CuPc and MnPc, deposited one after the other on the same Bi reconstructed substrate. The molecules self-assemble into a highly ordered bi-molecular array, as shown in Figure 21 C. The bimolecular mixture is perfectly sorted into an alternating pattern in 1:1 ratio. There is also a change in the contrast of molecules, with MnPc appearing brighter and CuPc appearing darker. We attribute this contrast enhancement to molecular doping as evidenced for other systems in earlier works. Doping of molecules can modify their electronic configuration, change the electrical conductivity and might also lead to changes in their magnetic moment [71]. Doping mechanisms are not fully understood at the single molecule level, however, recently STM demonstrated the capability to assist in such understanding, especially of transition metal phthalocyanines at metal surfaces [70].

If we provide an excess of CuPc, we observe that it substitutes MnPc, as can be seen in the black dotted circle in Figure 21 C. During our measurements, the opposite behavior, i.e.

MnPc substituting CuPc in the assembled array was never observed. Comparing the orientation of the molecules in the co-assembly with the orientation of single molecular islands, we observe that every MnPc molecule in the co-assembly exhibits lobes oriented along the main directions of Bi/Cu(100), denominated here as red cross. When MnPc is deposited individually, it exhibits two orientations of the islands: Lobes arranged along the main directions of the reconstruction or lobes arranged along a line rotated by 45° from the main crystallographic axes. CuPc exhibits two molecular orientations when deposited individually with the lobes aligned along the reconstruction and with the lobes oriented along a line forming a relative angle of 8° with the main directions. In the co-assembly, CuPc is oriented in the latter way (molecule marked by a green cross in Fig. 21). This observation reveals that the coexistence of both Pc families induces an orientation crossover. Since the Pcs used in our experiments did not possess any functional groups, no induction of chemical bonding can take place. Therefore, this chessboard arrangement suggests to be driven by electronic interactions. The interaction between nearest neighbors should also play a key role, since the pattern across the island is perfectly sorted between MnPc and CuPc.

In order to unravel the mechanisms of molecular nucleation and ordering leading to the self-sorting of two different molecular species, we performed STS and $I(z)$ spectroscopies of both species in single islands and also in the co-assembly, so that they can be compared. The first results shown here are discussed in terms of the energy levels of molecules as they are probed by STS.

Since the interaction between Pcs occurs via their ligands, we probed the local density of states of each molecule by recording the dI/dV spectra on the benzene ring. We have measured STS in the range of $-2V$ to $2V$ for single component Pcs islands and also for the co-assembly for comparison (Figure 22), in order to assign the charge transfer channels. It is important to note that all spectra were processed in a way such that the Bi/Cu(100) background, shown in Figure 20 B, had been removed and were normalized for better comparison.

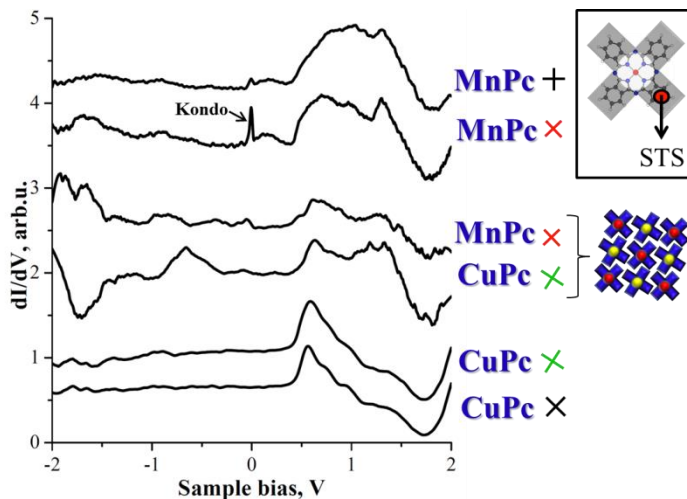


Figure 22: In order to understand the self-sorting mechanisms, the electronic structure of each component was probed by STS on the benzene ring of every molecule, so that only the ligand is probed. STS of MnPc and CuPc in single component islands was measured for all the orientations (marked by colorful crosses), and for molecules in the co-assembled array. In co-assembly, the electronic structure of both molecules has changed. STS was performed with 8 mV (zero-to-peak value), frequency of 513 Hz and set point parameters of 300 pA and 2V.

The single component self-assemblies of MnPc show a distinct behavior depending on the adsorption orientation. MnPc exhibits a HOMO/LUMO gap of approximately 2.2 eV (black cross) and 2.3 eV (red cross). We also observed a Kondo peak (shown in Figure 22) [72], the discussion of which lies outside of scope of this thesis. The single component assemblies of CuPc exhibit very similar features for both orientations except from minor differences (0.05 eV) in the LUMO and in the vibrational peaks, which shall also not be further treated in this thesis.

Quantitatively it is possible to observe differences in the STS spectra shown in Figure 21. Co-assembled molecules can be compared to single component islands of the two molecules as it has been done in Figure 23, in particular in the zoom section. From now on, we will compare the STS of molecules with the same orientation in single component assemblies (SCA) and in the bi-component co-assemblies (BCA), as shown in Figure 22. The peak position of the LUMO (0.58 eV) of SCA CuPc is similar to the position reported in literature for CuPc/NaCl/Cu(100) in neutral state [73], whereas the HOMO peak is not observed within the measured range [-2, 2] V. This means that the HOMO-LUMO gap is at least 2.5 eV. This lower bound for the gap presents a similar value to the one reported for CuPc by Swart, et al [73]. Comparing the LUMO position between SCA and BCA CuPc, we observe a shift of 0.1 eV to higher energies (Figure 23 A). This

observation indicates that the CuPc ligand, when co-assembled, is negatively charged. The explanation to this phenomenon is that the repulsion between molecular orbitals is then higher.

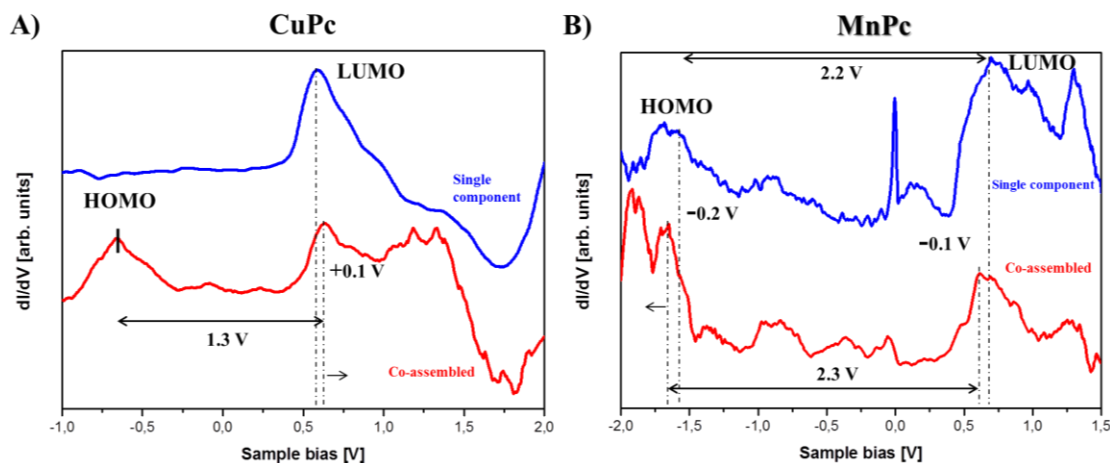


Figure 23: STS spectra for CuPc (A) and MnPc (B) in their single component and co-assembled component assemblies (called in the text SCA and BCA, respectively). A) The LUMO peak of CuPc shifts 0.1 eV to higher energies when co-assembled, which can be explained due to it being negatively charged. The HOMO-LUMO gap in the SCA CuPc is similar to the reported for CuPc anion [73].

As can be observed in Figure 23 B, the LUMO position of MnPc is shifted to lower energies between SCA and BCA. Therefore, when co-assembled, the MnPc ligand is positively charged. Another fingerprint of the positive charge of MnPc is that the HOMO peak exhibits splitting, which is explained by the electronic redistribution induced in the molecule [75]. Therefore, we can infer on the existence of interactions between the molecules across their benzene rings. This lateral interaction suggests to be what maintains the co-assembly cohesive. Besides the shifts of the LUMO peaks in MnPc and CuPc, the HOMO-LUMO gap between the SCA and BCA molecules changes. For MnPc, the gap was 2.2 V in SCA configuration and it changed to 2.3 V in BCA. CuPc exhibits a gap bigger than 2.5 V in SCA and it became 1.3 V in BCA. This reflects changes in the molecular orbitals induced by long-range electrostatic interactions [71].

The change in the interface electronics, i.e. formation of interface dipoles can influence the adsorption distances and modify the work function of the system [75]. In order to better understand the behavior of the co-assembled islands, we performed $I(z)$ spectroscopy measurements. The data was processed in order to generate work function maps of pure CuPc and MnPc islands, as well as of the co-assembled islands on Bi/Cu(100). The work function of the substrate was set to zero, since only relative differences can provide electronic information in our case.

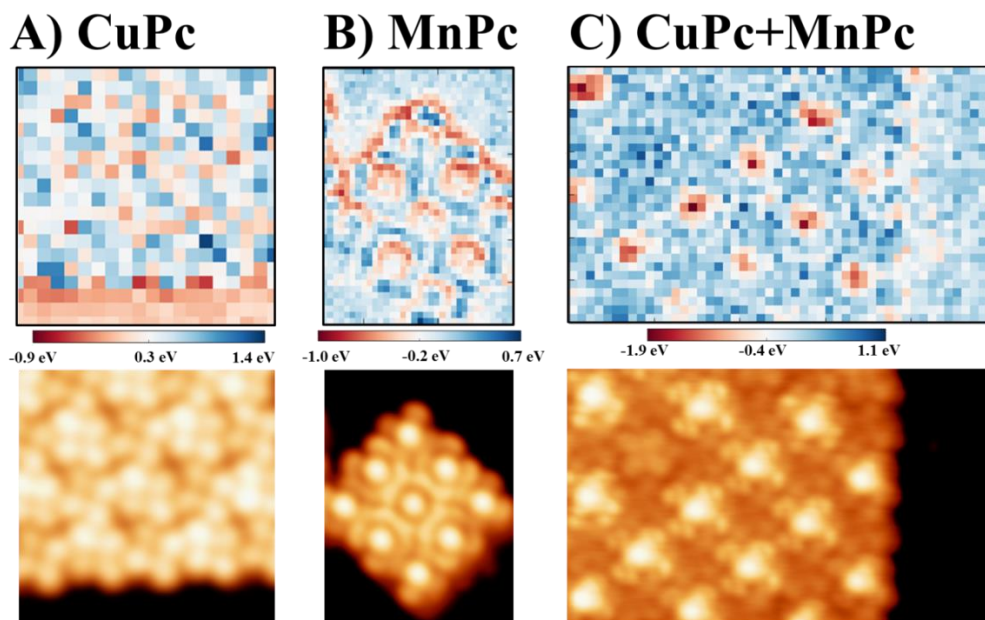


Figure 24: Comparison of the $I(z)$ maps for pure a) CuPc ($6 \times 6 \text{ nm}^2$) and b) MnPc ($12 \times 6 \text{ nm}^2$) islands, as well as c) co-assembled ($5 \times 6 \text{ nm}^2$) mixed arrays on porous bismuth reconstruction.

Operationally, we perform STM measurements on a given island and then create a grid with several places along the grid where the $I-z$ spectroscopy would be performed. Then we process every $I-z$ curve at every grid point and obtain a work function value. Subsequently, we calculate a new work function map, only accounting for the differences in work functions in comparison to the averaged work function of the Bi/Cu(100) surface. Thereby we create relative work function maps as shown in Figure 24. For these maps, we have assigned the centers of different molecules from the STM images and averaged the work function across 3×3 pixels of the map around the metal center position. The reason for this is that we do not possess enough resolution to locate the different components of lobe and center. These values for each molecule are described in Table 2. During the measurements, it was confirmed that the reference work function of the substrate remained approximately the same compared to the one measured before the start of the experiment on the bare substrate.

When $I(z)$ spectroscopy is performed on a thin film on top of a substrate, there are three factors, which influence the data: the tip, the thin film and the substrate. The influence of the tip has, in a first approximation, been removed from this problem by only comparing differences (considering that the tip can be considered the same within one round of experiments or that tip changes are usually spontaneously occurring and can thereby be identified in the 2D maps in a

straightforward way). Therefore, differences in the work function of the bismuth surface and of molecules on top of the bismuth surface can be associated to electronic effects: e. g. to an electron acceptor in the form of an adsorbate residing on top of the substrate. An acceptor here will induce a dipole pointing out of the surface, while an electron donor will result in the opposite behavior [76]. Moreover, these differences can be used to understand the existence of vertical charge transfers.

Table 2 demonstrates that the relative work function on SCA MnPc (red cross in Figure 20) amounts to $-(0.14 \pm 0.12)$ eV, which suggests a dipole moment in the center of the molecule pointing out of the surface, as schematically shown in Figure 25 B. When co-assembled, the relative work function in the center of the MnPc molecules is equal to (1.60 ± 0.04) eV. The relative work function $\Delta\phi$ is proportional, in first approximation, to the effective dipole moment [77], meaning that there is an increase of approximately 10 times in the dipole moment located underneath the MnPc molecule in the CCA when compared to the same molecule in SCA.

For SCA CuPc, the relative work function difference is $+(0.35 \pm 0.06)$ eV. As pointed out before, this can be understood as the adsorption of CuPc yielding a dipole moment pointing towards the surface, schematically shown in Figure 25 A. The co-assembled CuPc on Bi/Cu(100), on the other hand, exhibits a relative work function of $+(0.08 \pm 0.04)$ eV, which can be understood as if the dipole moment is oriented in the same direction, but diminished four times in strength. Therefore, depolarization of CuPc occurs upon mixing with MnPc.

Table 2: Relative work function change depending on the molecule and island type analyzed.

Island Type Molecule	Single component assembly	Co-assembled component assembly
MnPc	$-(0.14 \pm 0.12)$ eV	$-(1.60 \pm 0.04)$ eV
CuPc	$+(0.35 \pm 0.06)$ eV	$+(0.08 \pm 0.04)$ eV

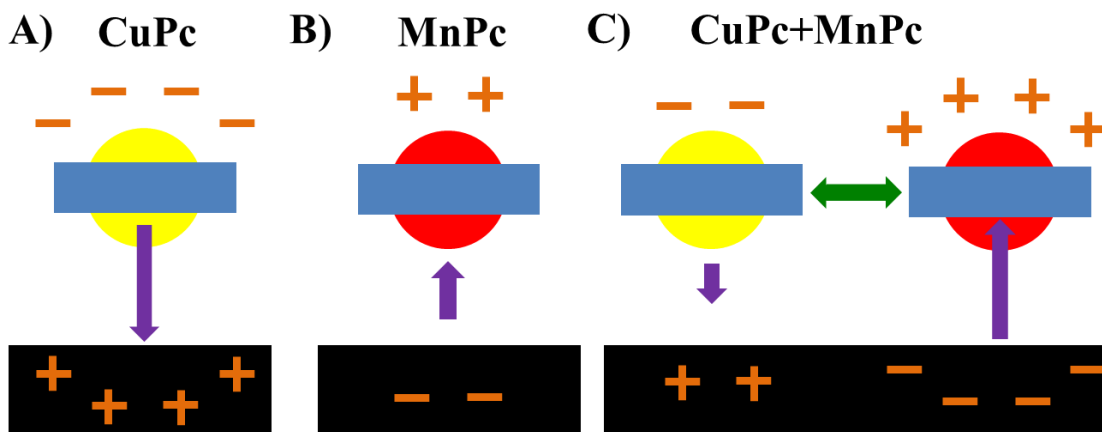


Figure 25: Schemes representing the interaction between the molecules and the substrate and the neighbouring molecules. A) Dipole moment pointing into the surface for single molecule islands of CuPc. B) Dipole moment pointing out of the surface for single molecule islands of MnPc. C) Change in dipole moment intensity when CuPc and MnPc are interacting with each other in the co-assembly.

We propose that the self-assembly of CuPc and MnPc in a 1:1 ratio is the result of two contributions: the existing vertical charge transfer between the two different molecules and the respective area of the substrate at which interaction takes place and different doping of the molecular ligands (Figure 25 C). We note that more studies are needed towards a better understanding of the mechanisms involved in the formation of this remarkable bi-molecular self-assembly pattern.

4.6 CONCLUDING REMARKS

In this chapter we have shown, by using scanning tunneling microscopy and spectroscopy, that CuPc and MnPc when deposited alone, self-assemble in islands. These islands exhibit different orientation and contrasts depending on their relative orientation with regard to the Bismuth reconstruction. By codeposition of MnPc and CuPc, it is possible to create a bimolecular mixture that self-assembles in a 1:1 ratio. This is due to either the energy levels re-alignment of the MnPc and CuPc or to electrostatic interactions between the dipoles.

Further experiments are also needed towards a better understanding on the internal electronic configuration of the molecules, which would enhance the knowledge about the nature of

the lateral interactions. Techniques such as High-resolution Atomic Force Microscopy and X-Ray Photoelectron Spectroscopy could possibly contribute to a further in-depth analysis. The former technique may provide further information on the conformation of the molecule, as well as it can probe the bonding limits between molecules and molecules and the substrate. The latter technique may be used to compare the binding energies between single island molecules and their co-assembled counterpart and infer on the metal's state, for example.

5 CONCLUSION AND PERSPECTIVES

Throughout this thesis, we have worked with two types of molecules: porphyrins and phthalocyanines. Both molecules have had their possible assemblies investigated on a wide range of (at the time available) metal substrates. We have used Scanning Probe Microscopy and Spectroscopy along with X-Ray Photoelectron Spectroscopy in this thesis. These techniques have allowed proper measurement of the structural and also electronic properties of the assemblies.

In terms of controlling molecular structures, we have demonstrated the capability of creating molecular lines of NiTPP along the step edges of low Miller index substrates - Cu(111) - and vicinal substrates - Au(332) and Au(788). This paves the way for future systematic studies on the magnetic properties of molecules attached to the step edges and the emergence of 1D magnetism over gas adsorption. The correct choice of Pcs and substrate (Bi/Cu(100)) yielded a chessboard that is 1:1 sorted in a quick and costly fashion. Such behavior creates the opportunity for big islands creation and also easier routes towards the construction of gas-adsorbate components, examples of future studies are the adsorption of small molecules such as CO or NO into this MnPc/CuPc co-assembly, in a similar way as it was performed by Wackerlin *et al* [28], this time without suppression of the magnetic states due to the adsorption of oxygen into the chamber.

Besides the study of applications for the devices towards future applications in gas sensors, more knowledge is needed towards the full understanding on the exact mechanism that led to the chemical shift of the Ni 2p core level of NiTPP on Cu(111) when compared to the NiTPP alone. We have collaborated with Prof. Roberto Hiroki Miwa (UFU) and Roberto Veiga (USP) to try to unravel such behavior.

It is also necessary to better understand the sorting dynamics of Pcs on the bismuth reconstructed surface. Although evidences suggest lateral electrostatic interactions and also dipolar change on the substrate, different experiments are needed: we suggest that performing XPS and High-resolution Kelvin Probe Microscopy would allow such understanding. The first technique, if possible to collect high-intensity signals, would enable to observe chemical shifts of the Mn and Cu core levels as well as characterizing the width of carbon and nitrogens. The second technique would provide enough resolution to observe inner electric potentials on the molecules while assembling, and it should be a much better technique for probing work function-like measurements. Our results also provide background for the fact that possibly the maximization of C-

H•••F interactions does not fully explain why fluorinated and regular Pcs co-assembly, where the substrate might act as a doping template in the same manner as it occurs with Bi/Cu(100).

Continuing on the perspectives of the co-assembly, we have decided, due to the compact form of a dissertation, to shown here one possible reconstruction of Bi/Cu(100) – p(10x10). There is another possible reconstruction, which will be called here p9, where instead of pores you have the creation of bismuth mazes. Further data is needed to obtain the same set of information presented here. What is known so far is that instead of a 1:1 chessboard array, we obtain a 1:2 (MnPc:CuPc) ratio, but structurally this assembly has several degrees of difficulty: huge unit-cell (16 molecules), mirrored domains and difference between electronic density of same molecules.

6 REFERENCES

- [1] R. P. Feynman, *There is Plenty of Room at the Bottom*, edited by H. D. Gilbert, H, Reinhold Publishing, New York, 1961.
- [2] G. Binnig, H. Rohrer, Ch. Gerber, E. Weibel, *Physical Review Letters* 49(1), 57-61, 1982.
- [3] J. S. Wall, J. Langmore, M. Isaacson, A. V. Crewe, *Proceedings of the National Academy of Sciences*, 71, 1-5, 1974.
- [4] D. M. Eigler, E. K. Schweizer, *Nature* 344, 524-526, 1990.
- [5] A. J. Heinrich, C. P. Lutz, J. A. Gupta, D. M. Eigler, *Science* 298, 1381, 2002.
- [6] National Nanotechnology Initiative
http://www.nano.gov/sites/default/files/pub_resource/2014_nni_strategic_plan.pdf
- [7] A. K. Geim, *Science* 324, 1530–1534, 2009.
- [8] A. Ulman, *Chemical Reviews*, 96, 1533, 1996.
- [9] A. Kuhnle, T. R. Linderoth, B. Hammer, F. Besenbacher, *Nature*, 415, 819, 2002.
- [10] C. Wackerlin, J. Nowakowski, S.-X. Liu, M. Jaggi, D. Siewert, J. Girovsky, A. Shchyrba, T. Ha'hlen, A. Kleibert, P. M. Oppeneer, F. Nolting, S. Decurtins, T. A. Jung and N. Ballav, *Advanced Materials*, 2013, 25, 2404–2408.
- [11] D. Grumelli, B. Wurster, S. Stepanow, K. Kern, *Nature Communications*, 4, 2904, 2013.
- [12] A. Schyrba, Ch. Wackerlin, S. Fatayer, Th. Nijs, S. Nowakowska and T. A. Jung, in preparation.
- [13] G. Binnig, H. Rohrer, Ch Gerber, E Weibel, *Physical Review Letters* 50(2), 120-123, 1983
- [14] J. A. Strosio, *Scanning Tunneling Microscopy*, Academic Press Inc, New York, 1994.
- [15] J. Chen, *Introduction to Scanning Tunneling Microscopy*, Oxford University Press, New York, 1993.
- [16] J. Tersoff, D.R. Hamann, *Phys. Rev. B*, 31, 805, 1985.
- [17] D. Drakova, *Reports on Progress in Physics* 64, 205–290, 2001.
- [18] J. Klein, A. Léger, M. Belin, and D. Défourneau, *Phys Rev. B*, 7, 2336, 1973.
- [19] J. T. Li, W.-D. Schneider, R. Berndt, O. R. Bryant, S. Crampin, *Phys. Rev. Lett.*, 81, 4464, 1998.
- [20] P. H. Lippel, R. J. Wilson, M. D. Miller, Ch. Woll, S. Chiang, *Physical Review Letters*, 62, 171, 1989.

- [21] D. A. Bonnell, D. N. Basov, M. Bode, U. Diebold, S. V. Kalinin, V. Madhavan, L. Novotny, M. Salmeron, U. D. Schwarz, P. S. Weiss, *Rev. Mod. Phys.* 84 1343-138, 2012.
- [22] K. Siegbahn, C. Nordling, A. Fahlman, R. Nordberg, K. Hamrin, J. Hedman, G. Johansson, T. Bergmark, S. E. Karlson, B. Lindgren, *ESCA Atomic, Molecular and Solid State Structure Studied by Means of Electron Spectroscopy*, Almquist Wiksells, Uppsala, 1967.
- [23] S. Tanuma, C. J. Powell, D. R. Penn, *Surf. Interface Anal.* 43, 689–713, 2011.
- [24] D. Briggs, M. P. Seah: *Practical Surface Analysis*, John Willey and Sons, New York, 1994.
- [25] A. Y. Cho, J. R. Arthur, *Prog. Solid State Chem.* 10: 157–192, 1975.
- [26] L. Gross, F. Mohn, N. Moll, B. Schuler, A. Criado, E. Guitián, D. Peña, A. Gourdon, G. Meyer, *Science* 337(6100), 1326-1329, 2012.
- [27] J.V. Barth, G. Costantini, K. Kern, *Nature* 437, 671-679, 2005.
- [28] C. Waeckerlin, D. Chylarecka, A. Kleibert, K. Mueller, C. Iacovita, F. Nolting, T. A. Jung, N. Ballav, *Nature Communications*, 1, 61, 2010.
- [29] D. H. Karweik, N. Winograd, *Inorganic Chemistry*, 15, 2336, 1976.
- [30] H. Nakashima, J.-Y. Hasegawa, H. J. Nakatsuji, *Computational Chemistry*, 27, 426, 2006.
- [31] B. Schuler, W. Liu, A. Tkatchenko, N. Moll, G. Meyer, A. Mistry, D. Fox, L. Gross, *Physical Review Letters*, 111, 106103, 2013.
- [32] D. G. Banhatti, *Journal of Astrophysics and Astronomy*, 16, 149, 1995.
- [33] M. Chen, X. Feng, L. Zhang, H. Ju, Q. Xu, J. Zhu, J. M. Gottfried, K. Ibrahim, H. Qian, J. J. Wang, *Journal of Physical Chemistry C*, 114, 9908, 2010.
- [34] Z.-Y. Yang and C. Durkan, *Surface Science*, 604, 660, 2010.
- [35] T. Kamikado, T. Sekiguchi, S. Yokoyama, Y. Wakayama, S. Mashiko, *Thin Solid Films* 499, 329, 2006.
- [36] X. Lu, K. J. Hipps, *Journal of Physical Chemistry B*, 101, 5391– 5396, 1997.
- [37] G. Lieve, L. Teugels, S. J. Sibener, *The Journal of Physical Chemistry C*, 115 (6), 2826, 2011.
- [38] J. Brede, M. Linares, S. Kuck, J. Schwobel, A. Scarfato, S. H. Chang, G. Hoffmann, R. Wiesendanger, R. Lensen, P. H. J. Kouwer, J. Hoogboom, A. E. Rowan, M. Broring, M. Funk, S. Stafstrom, F. Zerbetto, R. Lazzaroni, R., *Nanotechnology*, 20,275602, 2009.

- [39] W. Auwärter, K. Seufert, F. Klappenberger, J. Reichert, A. Weber-Bargioni, A. Verdini, D. Cvetko, M. Dell'Angela, L. Floreano, A. Cossaro, G. Bavdek, A. Morgante, A. P. Seitsonen, J. V. Barth, *Physical Review B*, 81, 245403-1– 14, 2010.
- [40] P Donovan, A Robin, M S Dyer, M Persson, R Raval, *Chemistry-European Journal*, 16, 11641, 2010.
- [41] E. B. Fleischer, C. K. Miller, and L. E. Webb, *Journal of the American Chemical Society*, 86, 2342, 1964.
- [42] M. E. Kosal and K. S. Suslick, *Journal of the American Chemical Society*, 89, 3331, 1967.
- [43] A. Weber-Bargioni, J. Reichert, A. P. Seitsonen, W. Auwaerter, A. Schiffrin, J. V. Barth, *Journal of Physical Chemistry C*, 112, 3453, 2008.
- [44] R. Domnick, G. Held, H.-P. Steinruck, *Surface Science*, 516, 95, 2002.
- [45] K. Flechtner, A. Kretschmann, H. P. Steinruck, J. M. Gottfried, *Journal of the American chemical Society*, 129, 12110–12111, 2007.
- [46] P. Gambardella, A. Dallmeyer, K. Malti, M.C. Malagoil, W. Eberhardt, K. Kern, C. Carbone, *Nature*, 416, 301, 2002.
- [47] S. Joshi, D. Ecija, R. Koitz, M. Iannuzzi, A.P. Seitsonen, J. Hutter, H. Sachdev, S. Vijayaraghavan, F. Bischoff, K. Seufert, J.V. Barth, W. Auwärter *Nano Letters*, 12 (11), 5821–5828, 2012.
- [48] G. Ehrlich, F.G. Hudda, *Journal of Chemical Physics*, 44, 1039, 1966.
- [49] E. Williams, *Surface Science*, 300, 502, 1994.
- [50] R. Smoluchowski, *Physical Review*, 60, 661, 1941.
- [51] A. Mugarza, A. Mascaraque, V. Perez-Dieste, V. Repain, S. Rousset, F. J. Garcia de Abajo, J. E. Ortega, *Physical Review Letters*, 87,107601, 2001.
Phys. Rev. Lett. 87 107601
- [52] M. J. Prieto, E. A. Carbonio, S. Fatayer, R. Landers, A. de Siervo, *Journal of Physical chemistry chemical physics*, 16, 13329-13339, 2014.
- [53] Y. Hasegawa, P. Avouris, *Science*, 258, 1763-1765,1992.
- [54] V. Repain, G. Baudot, H. Ellmer, S. Rousset, *Journal of Europhysics Letters*, 58, 730, 2002.
- [55] J. Kröger, N. Néel, H. Jensen, R. Berndt, R. Rurali, N. Lorente, *Journal of Physics: Condensed Matter* 18, S51, 2006.
- [56] V. Iancu, A. Deshpande, S. W. Hla, *Nano Letters*, 6, 820– 823, 2006.

- [57] D. Drolet, D. M. Manuta, A. J. Lees, A. D. Katnani, G. J. Coyle, *Inorganica Chimica Acta*, 146, 2, 173-180, 1988.
- [58] L. Scudiero, D. E. Barlow, U. Mazur, K. W. Hipps, *Journal of the American Chemical Society*, 124 (10), 2126-2127, 2001.
- [59] A. Braun, J. Tcherniac, *Berichte der Deutschen Chemischen Gesellschaft*, 40, 2709, 1907.
- [60] J. K. Gimzewski, E. Stoll, R. R. Schlittler, *Surface Science*, 181, 267, 1987.
- [61] C. C. Leznoff, A. P. Lever. *Phtalocyanines: Properties and applications*, VHC Publishers, New York, 1996.
- [62] K. W. Hipps, X. Lu, X. D. Wang, U. Mazur, *The Journal of Physical Chemistry* 100, 27, 11207-11210, 1996.
- [63] H.L Meyerheim, *Surface Science*, 418, 295–302, 1998.
- [64] P. Wynblatt, *Surface Science*, 601, 1623–1629, 2007.
- [65] P. Gargiani, M. G. Izzo, F. Bussolotti, M. G. Betti, S. Achilli, M. I. Trioni, *Journal of Chemical Physics*, 132, 174706, 2010.
- [66] M. Kaack, D. Fick, *Surface Science*, 342, 111, 1995.
- [67] F. Schulz, R. Drost, S. K. Hämäläinen, P. Liljeroth, *ACS Nano*, 12, 11121-11128, 2013.
- [68] P. Järvinen, S. K. Hämäläinen, K. Banerjee, P. Häkkinen, M. Ijäs, A. Harju, P. Liljeroth, *Nano Letters*, 13, 3199–3204, 2013.
- [69] S. Joshi, F. Bischoff, R. Koitz, D. Eciija, K. Seufert, A. P. Seitsonen, J. Hutter, K. Diller, J. I. Urgel, H. Sachdev, J. V. Barth, W. Auwärter, *ACS Nano* 8, 430, 2014.
- [70] C. Krull, R. Robles, A. Mugarza, P. Gambardella, *Nature Materials*, 12, 337–343, 2013.
- [71] M. F. Craciun, S. Rogge, A. F. Morpurgo, *Journal of the American Chemical Society*, 127, 12210–12211, 2005.
- [72] K. J. Franke, G. Schulze, J. I. Pascual, *Science*, 332, 940, 2011.
- [73] I. Swart, T. Sonleitner, J. Repp, *Nano Letters* 11, 1580, 2011.
- [74] J.-Q. Zhong, X. Qin, J.-L. Zhang, S. Kera, N. Ueno, A. T. S. Wee, J. Yang, W. Chen, *ACS Nano*, 140116123939006, 2014.
- [75] P. Ruffieux, K. Ait-Mansour, A. Bendounan, R. Fasel, L. Patthey, P. Gröning, O. Gröning, *Physics Review Letters*, 102, 2009.
- [76] P. S. Bagus, D. Kaefer, G. Witte, C. Woell, *Physical Review Letters*, 100, 126101, 2008.

[77] E. Goiri, M. Matena, A. El-Sayed, J. Lobo-Checa, P. Borghetti, C. Rogero, B. Detlefs, J. Duvernay, J. E. Ortega, D. G. de Oteyza, *Physical Review Letters*, 112, 2014.